IceCube-Gen2 cascade reconstruction studies with the PDOM and mDOM

Bachelorarbeit aus der Physik

Vorgelegt von
Sebastian Spiegel

13. Juli 2018

Erlangen Centre for Astroparticle Physics
Friedrich-Alexander-Universität Erlangen-Nürnberg

Betreuer: Prof. Dr. Gisela Anton, Dr. Thorsten Glüsenkamp

ERLANGEN CENTRE
FOR ASTROPARTICLE
PHYSICS

ICECUBE
GEN2

Abstract

Several new designs of digital optical modules (DOMs) have been proposed and are currently under development for IceCube-Gen2, the planned extension of the IceCube South Pole Neutrino Observatory. An important detection channel in IceCube are electromagnetic showers that can be induced by various processes. In this thesis, directional reconstructions of electromagnetic showers for Gen-2 geometries equipped with PDOM and mDOM are compared with respect to their angular errors, using two different likelihood approaches. This is done for both realistically propagated photons and idealized photons that are drawn from the expected PDFs. The examined dataset contains cascades in the 10 TeV – 10 PeV energy range. The angular errors over neutrino energy for all reconstructions lie in a range between $\sim 17^\circ$ and $\lesssim 2^\circ$ while an improvement with increasing energy is perceptible. The cascade reconstructions for the mDOM yield up to $\sim 50\%$ better angular errors compared to the PDOM in the low- and mid-energy regime. The results apply to the idealized pulses and some technical challenges remain for investigation in future studies.

Contents

1 Introduction

Astronomy has always been an important part of mankind since ancient history. It enabled scientists for example to describe and even predict the movements of the planets in our Solar System. Among other discoveries, it lead Isaac Newton to his formulation of the gravitational law and classical mechanics, concepts which had an astonishing influence on technology, and therefore everyday life.
Examples like this show that the study of phenomenons which seem far-fetched at first can lead to discoveries with major impact on mankind. Space is like a playground for physical theories as it's providing possibilities to examine them under extreme conditions like in Supernovae or **a**ctive **g**alactic **n**uclei (**AGN**).
In recent years, new fields of research like the detection of gravitational waves and Neutrino Astrophysics have emerged.
Neutrino astrophysics provides new possibilities due to the fact that neutrinos interact very weakly and can travel through matter or electromagnetic fields without being absorbed, scattered or attenuated. Thus, neutrinos can travel cosmic distances, escape optically thick sources and point back to their source. All of these factors mark big advantages in contrast to traditional photon-based astronomy.
The discovery of point sources is a crucial goal in Neutrino Astronomy. On the one side, it would open up a new channel for astrophysical observation of objects which can't be observed with photon astronomy. On the other side, the allocation of neutrinos to an astrophysical object is an indisputable evidence for hadronic acceleration in the object due to the fact that neutrinos are produced by the interaction of accelerated nuclei with matter or electromagnetic fields.
The identification of such objects is a key issue in Astroparticle Physics as it might help to explain the origin and the acceleration mechanisms of the highest energy cosmic rays. As a logical consequence, experiments were and are built to exploit the advantages of neutrinos over photons. Nevertheless, the weak interaction of neutrinos leads to the necessity of enormous detectors.
Currently, the largest of them is the IceCube South Pole Neutrino Observatory which is located near the geographical south pole on earth. Its optical sensors are distributed over an array with the size of roughly $1\,\mathrm{km}^3$ deep in the Antarctic ice.
The detector measures Cherenkov light emitted from relativistic charged particles, traveling through the ice, which are produced by interactions between neutrinos and the ice. With this detection principle, IceCube managed to measure enough neutrinos to proof a diffuse cosmic neutrino flux in 2013. However, until today it is not possible to identify any point sources of neutrino emission.
There are several ways to improve the sensitivity to neutrino point sources: increase

the detection volume to measure more neutrinos and, therefore, get better statistical statements, improve the sensors of the detector or create better directional reconstruction methods.
The planned IceCube expansion Gen2 addresses the first two aspects. It adds more and improved sensors to the existing detector to increase the detection volume to $10\,\mathrm{km}^3$.
The improvement of directional reconstruction methods, however, is a continuous process and methods which were used for IceCube have to be adjusted for Gen2. To get reliable information about the suitability of reconstruction methods a high amount of reconstructed events is necessary. Through the reconstruction of simulated events true and the reconstructed event properties can be compared.
In this thesis, reconstruction studies of cascade events[1] for the proposed mDOM & PDOM[2] light sensors of the IceCube expansion Gen2 are carried out and compared. The directional reconstruction of cascade events is important since cascades are the dominant neutrino event topology in IceCube. The second chapter motivates the field of research of High-Energy Neutrino Astrophysics, explains the detection concept of the IceCube neutrino detector and emphasizes the importance of cascade events in this context. In chapter three, the IceCube South Pole Neutrino Observatory and its planned expansion Gen2 will be introduced. Hereby, the light sensor of IceCube itself and the two above-mentioned sensors for Gen2 are presented. Subsequently, the reconstruction method is explained in chapter four. Chapter five introduces the used dataset, the applied cuts and in which manner the light of the events was generated in order to acquire the investigated sample. The obtained results of the applied reconstruction method are presented and discussed in chapter six. Finally, a conclusion is drawn in chapter seven.

[1] light pattern produced by certain interactions channels of neutrinos with matter, compare section 2.3
[2] **DOM** = **d**igital, **o**ptical **m**odule, see chapter 3

2 High-Energy Neutrino Astrophysics

Neutrinos unique cosmic messengers and provide new opportunities to explore the universe.
This chapter motivates neutrino astrophysics and emphasizes how key questions in particle physics are addressed.
Moreover, the detection principle of the IceCube South Pole Neutrino Observatory shall be explained.

2.1 Cosmic rays

Even more than 100 years after the discovery of cosmic rays by Victor Franz Hess in 1912 [24] the location and manner of high-energetic cosmic ray production still remains unclear [35].
Cosmic Rays consist predominantly of protons with a fraction of roughly 80%. The remaining components are basically atomic nuclei (e.g. α particles, iron nuclei) with some traces of electrons and anti particles [43].
All the named particles have a charge and, therefore, can be deflected by magnetic fields on their journey through space [11]. This makes it difficult to allocate cosmic rays to their sources by the means of their arrival directions.
Measurements show that the energies of cosmic rays reach up to 10^{21} eV, compare fig. 2.1.
The following discussion of the cosmic ray energy spectrum is based on [35]:
The spectrum can be described by a broken power law of the form $E^{-\alpha}$. In the low energy range up to about 1 PeV, the power index equals 2.7 until the slope of the spectrum steepens at the so called "knee" to $\alpha = 3.1$. It is assumed that this first break in the spectrum is based on the transition from galactic to extragalactic accelerators. Nevertheless, there are known galactic processes which could possibly accelerate cosmic rays up to energies between 10^{17} and $10^{18.5}$ eV. For energies above $10^{18.5}$ eV the cosmic ray spectrum changes its slope back to $\alpha = 2.7$. This behavior is often referred to as the "ankle". Nearly all cosmic rays with higher energies must have an extragalactic origin due to the fact that their gyroradius exceeds the size of the milky way and, therefore would, even if produced in the Galaxy, escape it immediately. Ultimately the cut-off of the cosmic ray spectrum is probably explained best by the **G**reisen-**Z**atsepin-**K**uzmin cut-off („**GZK** cut-off“) which describes the production of the Δ^+-resonance due to the interaction of protons with the **c**osmic **m**icrowave **b**ackground (**CMB**) at energies

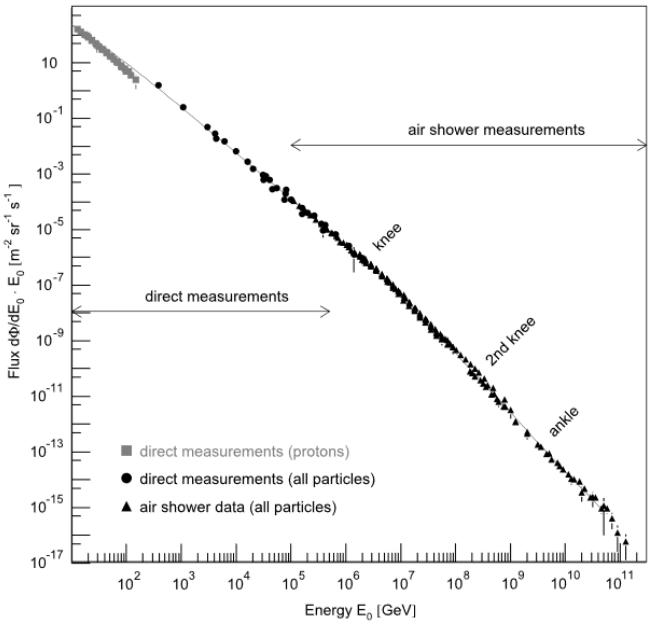

Figure 2.1: Energy spectrum of cosmic rays up to 10^{12} GeV with its characteristic features („knee“ and „ankle“). Taken from [8].

$\gtrsim 10^{19}$ eV:

$$p + \gamma_{\mathrm{CMB}} \rightarrow \Delta^{+} \tag{2.1}$$

, see fig. 2.2.
Thus, the question arises, which particular galactic and extragalactic sources accelerate cosmic rays?
On the galactic side, it is believed that the major contributor to cosmic particle acceleration are **s**uper**n**ova **r**emnants (SNR) [25][35]. Here, shock fronts from supernova explosions propagate into the interstellar medium and particles gain energy by multiple scattering between shock fronts. This mechanism is known as „first order fermi acceleration“ [15][7]. Furthermore, other sources could be pulsars and binary systems where one of the partners is a neutron star or a black hole [35].
Possible candidates for extragalactic sources are **A**ctive **G**alactic **N**unclei (AGN), **G**amma **R**ay **B**ursts (GRB) and starburst galaxies [6].

2.2 Neutrinos as cosmic messengers

Before addressing reasons which lead to the conclusion that neutrinos are cosmic messengers and in which manner neutrinos are produced it is argued why photons like the

previously mentioned protons[1] reach their limits, especially in terms of identifying cosmic ray sources.
The propagation of Photons in space is limited due to scattering with the CMB and the **c**osmic **i**nfra**r**ed **b**ackground (**CIRB**), see fig. 2.2 [26]. Thus, photons in the PeV energy regime can reach only distances of a few 100 kpc, the size of a galaxy. This is a drawback as photons in this energy range are not expected in leptonic processes and, therefore, would be an unambiguous evidence for hadronic acceleration in a source [37].

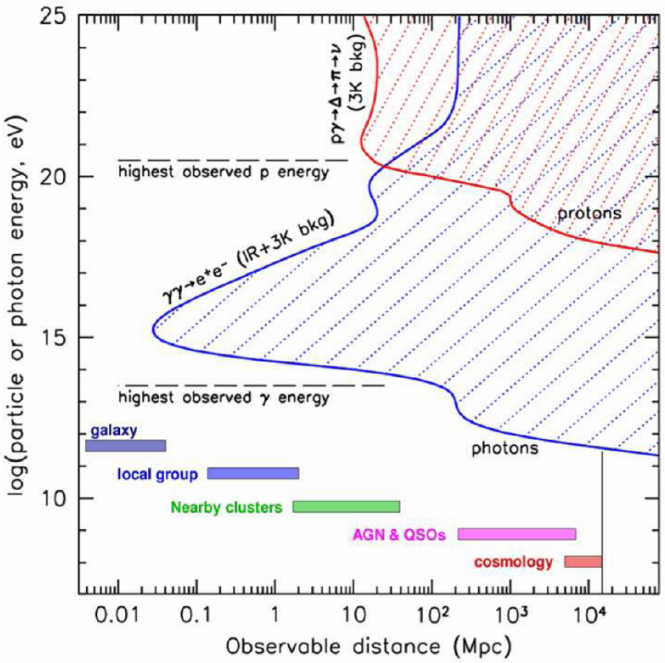

Figure 2.2: Propagation horizon of cosmic messenger particles dependant of their energy. Attenuation of photons by CMB & CIRB (blue) and attenuation of protons by the CMB (red). Taken from [26].

Neutrinos are nearly massless[2] particles which have neither an electric nor a color charge, almost[3] no magnetic moment and interact almost only weakly [10]. The cross sections $\sigma_{\nu p}$ for neutrino-nuclei interactions lie typically in the range of $10^{-38}\,\mathrm{cm}^2$ and increase with the neutrino energy [18]. These properties lead to the conclusion that neutrinos are ideal cosmic messengers since they can, therefore, escape optically thick sources, travel cosmic distances without interacting with the CMB and don't get deflected by magnetic fields [10]. Hence, neutrinos loose basically no information on the way from source to observer.

[1] or any other charged particle
[2] e.g. $m_{\bar{\nu}_e} < 2\,\mathrm{eV}$ [43]
[3] subject of current research, see for instance [4]

High-energy neutrinos are expected to be produced in hadronic accelerators due to the interaction of accelerated protons with surrounding matter or radiation fields:

$$p + nucleus \rightarrow \pi + X \quad \pi \in \{\pi^+, \pi^-, \pi^0\} \tag{2.2}$$

$$p + \gamma \rightarrow \Delta^+ \rightarrow \begin{cases} \pi^0 + p \\ \pi^+ + n \end{cases} \tag{2.3}$$

with the ensuing decays and their branching ratios

$$\pi^0 \rightarrow \gamma\gamma \qquad (98.823 \pm 0.034\%) \tag{2.4}$$
$$\pi^\pm \rightarrow \mu^\pm + \nu_\mu\,(\bar{\nu}_\mu) \qquad (99.98770 \pm 0.00004\%) \tag{2.5}$$
$$\mu^\pm \rightarrow e^\pm + \bar{\nu}_\mu\,(\nu_\mu) + \nu_e\,(\bar{\nu}_e) \qquad (\approx 100\%). \tag{2.6}$$

This makes the discovery of neutrinos in a point source to a clear evidence of hadronic acceleration [35],[43]. Furthermore, the just mentioned neutrino production channels imply a flavour ratio of roughly $\nu_e : \nu_\mu : \nu_\tau = 1 : 2 : 0$ at the source but due to neutrino oscillations, the flavour ratio on arrival at earth turns into $\nu_e : \nu_\mu : \nu_\tau = 1 : 1 : 1$ [35].
In conclusion, neutrino astronomy is an important element to understand the origin and acceleration mechanisms of cosmic rays.

2.3 Neutrino detection with Cherenkov detectors

All the advantages of neutrinos from section 2.2 hold the disadvantage that neutrinos are challenging to detect due to the fact that they only interact via weak interaction. Therefore, it is necessary to measure secondary particles to detect neutrinos. Their weak ability to interact is reflected by the small cross sections, for instance the neutrino-proton cross section [48]:

$$\sigma_{\nu p} \sim \frac{E_\nu}{\mathrm{GeV}} \cdot 10^{-38}\,\mathrm{cm}^2. \tag{2.7}$$

As a result of these small cross sections, large detectors are required to measure a statistical significant amount of neutrinos [23].
In IceCube, the dominant neutrino interactions in the detection material are basically deep-inelastic scatterings with nucleons via the **n**eutral **c**urrent (**NC**) or the **c**harged **c**urrent (**CC**) branches of the weak interaction[4] which is based on the mass of the interaction partner, energy and flavour of the incoming neutrino [10],[9], see also fig. 2.3a. The peak in fig. 2.3a is the so called Glashow resonance which describes the resonant scattering of $\bar{\nu}_e + e^- \rightarrow W^-$ but yet has not been detected with IceCube [46] and, therefore, won't be discussed here more explicitly.

[4] gauge bosons – NC: Z^0, CC: $W^\pm$

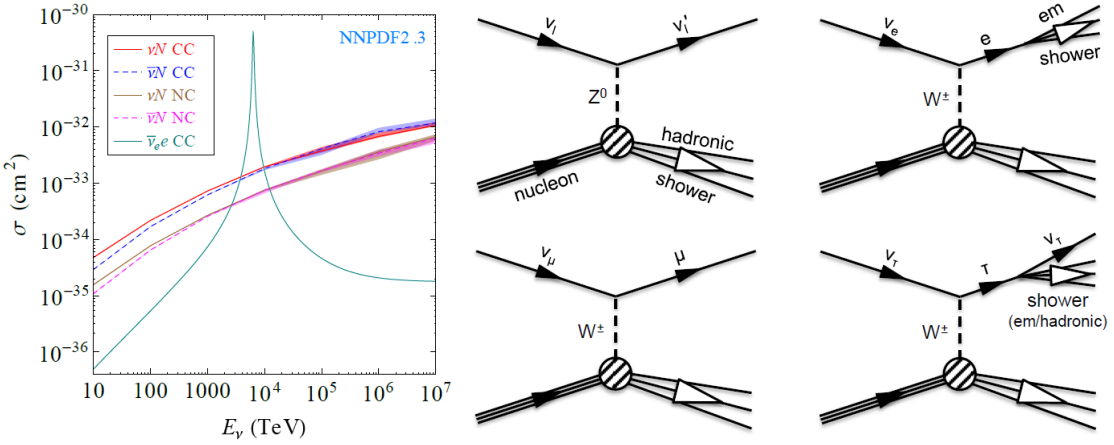

(a) (b)

Figure 2.3: **(a)** Computed dominant neutrino-induced interaction cross sections in the **S**tandard **M**odel (**SM**). Taken from [9]. **(b)** Schematic Feynman graphs of deep inelastic neutrino-nucleon interactions above GeV Energies. Taken from [10].

In these deep-inelastic neutrino-nucleon interactions, charged leptons l are produced [10],

$$\nu_l\,(\bar{\nu}_l) + nucleon \rightarrow l\,\left(\bar{l}\right) + X \quad \textbf{(CC)} \tag{2.8}$$

$$\nu_l\,(\bar{\nu}_l) + nucleon \rightarrow \nu_l\,(\bar{\nu}_l) + X \quad \textbf{(NC)} \tag{2.9}$$

where $l \in \{e, \mu, \tau\}$ and X denotes a hadronic component, possibly even a hadronic shower (see figure fig. 2.3b for the affiliated Feynman graphs).

In Cherenkov detectors like IceCube the charged particles, created in this kind of interactions, are detected via the Cherenkov effect [23].
The Cherenkov radiation is a phenomenon which occurs when a charged particle propagates through matter with a lager velocity v than the phase speed of light in the medium $\frac{c}{n}$ and can be seen as an optical analogue to the sonic boom. The atoms along the particle trajectory are polarized and if the stated velocity barrier is exceeded the excited spherical waves interfere coherent to a light cone. Hereby created photons can be measured in optical transparent media[5]. The opening angle θ of this so called Cherenkov cone is given by

$$cos(\theta) = \frac{1}{\beta \cdot n} \tag{2.10}$$

where $\beta = \frac{v}{c}$ and $n(\lambda)$ stands for the wavelength dependent refractive index of the crossed matter. Furthermore, the number of Cherenkov photons per path length x and per

[5] e.g. ice or water

wavelength λ can be calculated to

$$\frac{\mathrm{d}^2N}{\mathrm{d}x\mathrm{d}\lambda} = \frac{2\pi\alpha z^2}{\lambda^2}\left(1 - \frac{1}{\beta^2 \cdot n^2}\right) \tag{2.11}$$

with the fine structure constant α and the number z of elementary charges e that a charged particle carries. Thus, short wavelengths are prefered in the Cherenkov spectrum [39],[35],[23].
In CC-interactions of neutrinos the energy is transferred to the created lepton and the nucleon target, compare eq. (2.8). The latter produces in turn a hadronic shower. Both the lepton and the hadronic shower produce light via Cherenkov radiation. A hereby created muon in the $\mathcal{O}$(TeV) – $\mathcal{O}$(PeV) range leaves a kilometer-long track signature in the detection material until it decays [23].
Electrons and mostly taus as well as NC-interactions lead to the so called **„cascade event“** signature. Electrons interact after a short propagation length with the surrounding detection material and produce an electromagnetic shower which again emits light due to Cherenkov radiation. This makes it impossible to resolve the hadronic and the electromagnetic shower resulting in the detection of one coherent cascade. The event topology of the tau lepton is energy dependent as the decay length of the tau is energy dependent. For higher PeV energies the tau propagates several hundred meters until it decays, producing a second shower. This is called the „double bang“ signature. With lower energies the decay length of the tau decreases, making it more difficult to distinguish between the two showers. As a result the double bang signature has yet to be identified. The length of a cascade event increases with the logarithm of the cascade energy and is typically in the order of 5 – 20 m [35][23][14]. A illustration of track and cascade events can be found in fig. 2.4.

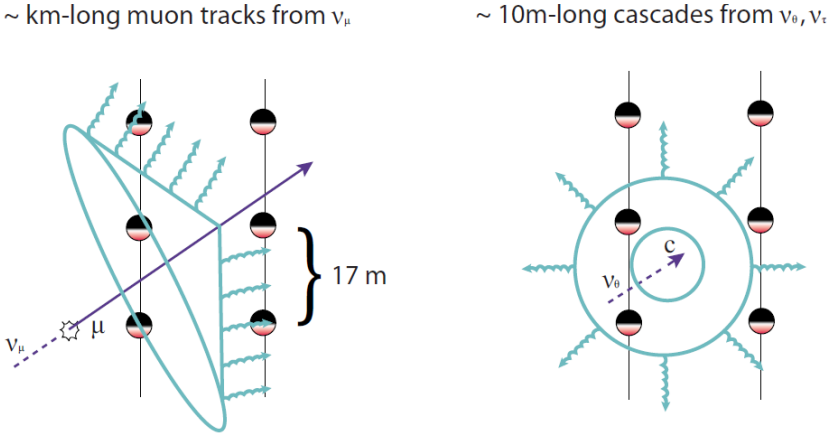

Figure 2.4: Event signatures in IceCube: Muon tracks created in **CC**-interactions with ν_μ **(left)** and cascades produced by **CC**-interactions from ν_e & ν_τ and **NC**-interactions **(right)**. Taken from [23].

3 IceCube South Pole Neutrino Observatory

The IceCube South Pole Neutrino Observatory is a kilometer-scale high-energy Water-Cherenkov detector based on the Cherenkov effect. It is localized near the Amundsen-Scott South Pole Station in Antarctica. IceCube is a multipurpose detector in the sense that it not only performs high-energy Neutrinoastrophysics with the In-Ice-Array but also investigates e.g neutrino oscillation parameters with its sub-array DeepCore and studies cosmic-rays with the air shower array IceTop [2], compare fig. 3.1.
This chapter focuses on composition, geometry and goals of the IceCube In-Ice Array and its planned high-energy extension, the High-Energy Array of IceCube-Gen2. In addition to that, the current and two possible future light sensors are presented.

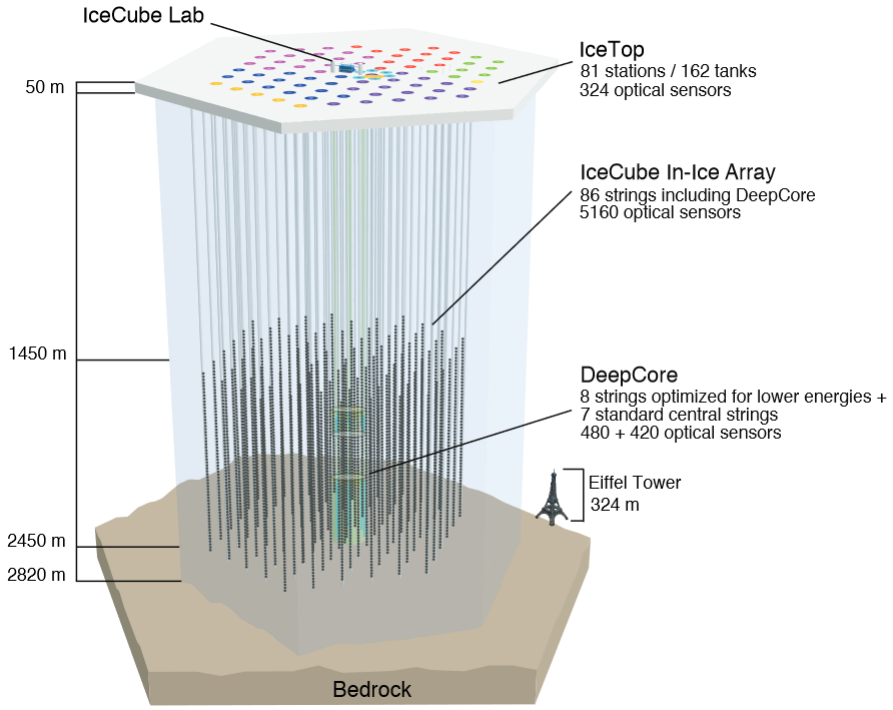

Figure 3.1: Schematic view of the IceCube South Pole Neutrino Observatory and its In-Ice Array, DeepCore and IceTop. Taken from [2].

3.1 IceCube In-Ice Array

The IceCube In-Ice Array is the main component of the IceCube South Pole Neutrino Observatory. It consists of 86 vertical strings deployed in the antarctic ice below the surface at a depth of 1450 – 2450 m [2]. This location was chosen as it provides suitable[1] optical ice properties in the ice layers at this depths in terms of light scattering and absorption[2] [23].
A total of 5160 **d**igital **o**ptical **m**odules (**DOM**s), which measure the Cherenkov radiation, are distributed on these strings. The horizontal spacing between the strings is mostly 125 m while the vertical spacing between the DOMs on a string are 17 m, leading to a hexagonal detection volume of roughly 1 km^3, see fig. 3.1. This geometric properties were chosen to optimize the detector for neutrino energies in the range of $\mathcal{O}$ (TeV) – $\mathcal{O}$ (PeV) [2].
The goals targeted with IceCube are measuring the neutrino energy spectrum in the stated energy range, detect high energy cosmic neutrinos and identify cosmic neutrino point sources to improve the understanding of cosmic rays [20].
Although no neutrino point sources could be identified yet due to insufficient statistics [1], a diffuse cosmic neutrino flux was discovered in 2013 [32] and confirmed until now with a significance of $> 6\sigma$ [50].
As the main intention of neutrino astronomy is to identify point sources in order to understand origin and acceleration mechanisms of cosmic rays, larger and newer detectors than IceCube are necessary to accomplish this goal. A possible realization of this requirements is the IceCube extension Gen2 [33], see section 3.3.

3.1.1 IceCube DOM

The IceCube DOM is light sensor and the main data acquisition instrument of the IceCube neutrino telescope. A schematic layout of the DOM is shown in fig. 3.4 and the basic operation principle is outlined in the following[3]. The hole device is encompassed by a spherical glass house to protect the technical components from high pressures and penetration of the surrounding ice. Incoming Cherenkov photons are detected by the 10" downward-facing **p**hoto**m**ultiplier **t**ube (**PMT**) which represents the core of the system [2]. Subsequently, the from the PMT measured waveforms are digitized by the main board due to information loss with analog signal transmission to the surface [23].
This digital signal is transmitted via the penetrator to the IceCube Lab, see fig. 3.1, on top of the ice where its further procession takes place [2].
Beyond, the instrumentation includes a LED flasher board to probe the ice properties as well as for calibration purposes, like verification of the time respones and measuring the position of the DOM [2].

[1] clear ice layers; in ice trapped air bubbles are compressed due to the high pressures [23]
[2] measured absorption length of blue light in antartic ice at a depth of 1450 – 2450 m: > 200 m [23]
[3] a detailed overview of the IceCube DOM can be found in [2]

3.2 Importance of cascade events in IceCube

Cascade events play an important role in IceCube. They are the dominant event topology in the detector. The reason for this are the above-mentioned dominant interaction channels of neutrinos with matter. Therefore, the only occuring channels leading to a track event are the CC-interaction from ν_μ's and extremely high-energy $\nu_t au$'s with nucleons. All other mentioned channels lead to cascade-like event signatures, produced by electromagnetic and hadronic showers in the ice [3].
Moreover, cascade events allow good energy reconstructions as they can be fully contained in the detector due to their compact event signature [40].
In the process of identifying cosmic neutrinos cascade signatures play a significant role. The so called **HESE**(**H**igh-**e**nergy **s**tarting **e**vent)-analysis is one possible way of filtering background events which consist of atmospheric muons and neutrinos produced by the interaction of cosmic rays with nuclei in the atmosphere. This type of event selection subsists of two analysis steps. The first one is the **starting event** selection. Here, a part of the detector is defined as a so called **veto region**, see fig. 3.2. Every event which deposits its first photons in this region is rejected. As a result only events which start in the detector are retained. This leads to the filtering of muon tracks of atmospheric origin since they begin to produce Cherenkov radiation in the ice on their path outside of the detector. The second step is a **high-energy** event selection which rejects events with energies under a certain threshold. This selection is based on the expectation that astrophysical neutrinos have a harder spectrum than the atmospheric neutrinos. The HESE-analysis was used in the discovery of the diffuse cosmic neutrino flux in 2013[4] [32].

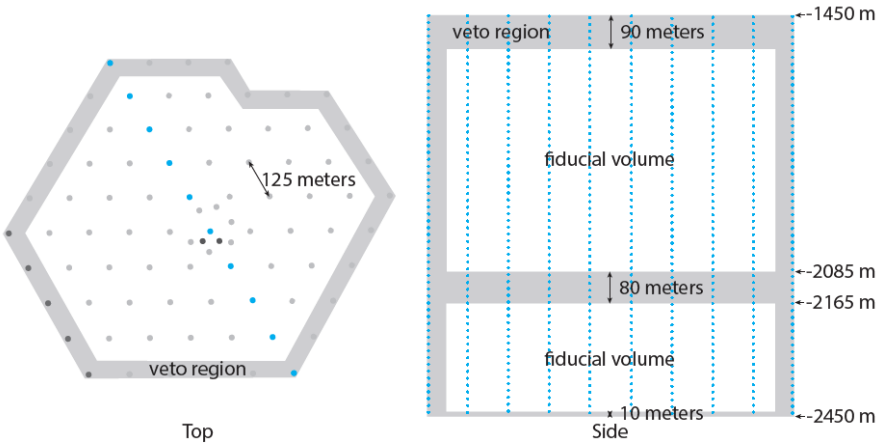

Figure 3.2: IceCube detector with veto region (grey) in top view **(left)** and side view **(right)**. Taken from [32].

A big drawback of cascade events are their bad angular errors of directional reconstruction

[4]dataset with 28 events from HESE-analysis consisting of 21 cascades and 7 tracks

in the range of $\sim 10 - 20°$ [3]. Therefore, directional reconstructions for cascade events are a topic of interest in order to better identify point sources with this detection channel.

3.3 IceCube-Gen2: High-Energy Array

IceCube-Gen2 is a proposed extension of the existing IceCube detector, see fig. 3.3. Among other components, this expansion includes a new detection Array with a size of approximately $7 - 10\,\mathrm{km}^3$, namely the High-Energy Array[5]. It will be realized by roughly doubling the currently operating strings, justified by the ice properties found in the IceCube detection volume [33].

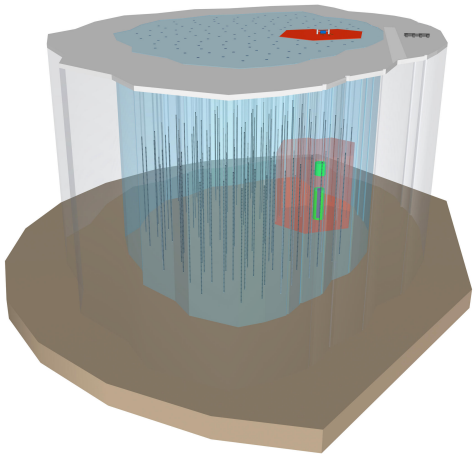

Figure 3.3: Schematic overview of IceCube-Gen2, including IceCube (red), the High-Energy Array (blue), DeepCore (purple) and PINGU (green). Taken from `https://gallery.icecube.wisc.edu/internal/`.

With this geometry the High-Energy Array aims at neutrino energies above 100 TeV. A primary goal of this experiment is the detection of a large amount of neutrinos above the stated energy threshold, allowing a better understanding of the astrophysical neutrino flux and more importantly the identification of neutrino point sources. The predicted size of the detector provides for instance also the potential of measuring GZK-Neutrinos which are produced in the decay of Δ^+ (compare eq. (2.1)) or Neutrinos from the Glashow resonance [33].

[5] final size depends on choosen DOM and string spacing

3.3.1 PDOM and mDOM

For IceCube-Gen2 several new DOM-designs have been considered and proposed. Two promising concepts are the **PDOM**[6] (**P**INGU **DOM**) and the currently developed **mDOM** (**m**ulti-PMT **DOM**) which shall be presented in the following [47],[10].
The PDOM is the continuation of the IceCube approach by harboring one 10"-PMT which is basically the same used in the low energy array DeepCore. DOMs in DeepCore hold a higher quantum efficiency than the modules in the rest of the IceCube In-Ice Array. The basic idea of this kind of detector design is to maintain the reliability and to use the empirical values provided by the DOMs used in IceCube on the one side and updating outdated and obsolete components on the other side. Differences between the PDOM and the IceCube-DOM are displayed in fig. 3.4 [47],[10].

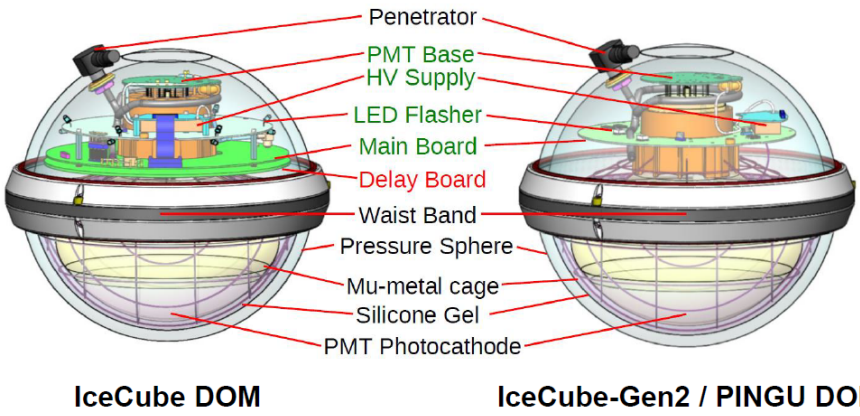

Figure 3.4: Schematic comparison of the IceCube-DOM **(left)** and the **P**INGU **o**ptical **m**odule (**PDOM**) **(right)**. Differences highlighted in colour. *Black* labels: identical components, *green* labels: redesigned components, *red* label: dismissed component. Taken from [10].

The mDOM concept distinguishes fundamentally from that of the PDOM and is based on the design of the optical module which was designed for KM3NeT. Instead of one downward-facing PMT with $\sim 2\pi$ coverage the mDOM houses 24 3"-PMTs with an angular acceptance of almost 4π, compare fig. 3.5. Furthermore, the effective photocathode area of the mDOM is more than doubled compared to the PDOM while the price per photocathode area is aimed to be equal. Exemplary advantages of this novel module design are, in addition to the higher photocathode area and the improved angular acceptance, better photon counting, an intrinsic directional sensitivity and the possible use of local coincidences to suppress noise like the dark rate [10],[36].

[6] often also referred to as **GEN2-DOM**, like for instance in [10]

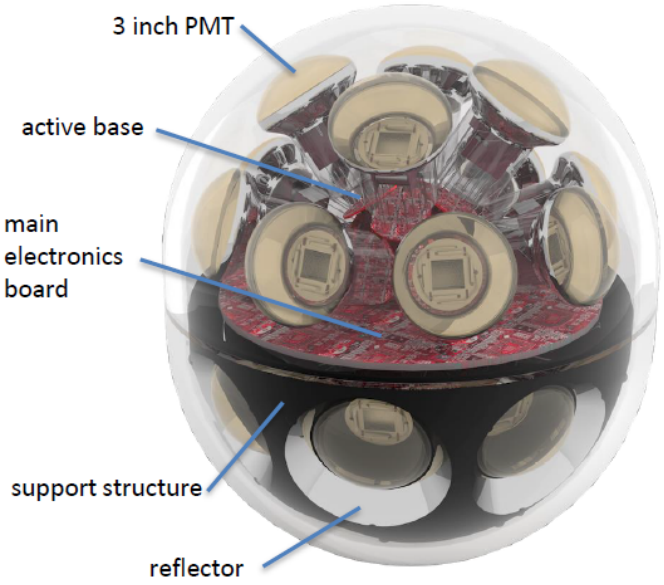

Figure 3.5: Artistic representation of the planned **m**ulti-PMT **o**ptical **m**odule (**mDOM**). Black support structure removed in upper hemisphere for illustration purposes of the internal components. Taken from [49].

4 Reconstruction methods

The fundamental physical quantities measured in IceCube are the number of photons arriving at a DOM and their arrival time. Thus, IceCube is basically a photon-counting experiment where the interesting neutrino properties have to be determined with the information about the counted photons. A general approach to reconstruct physical events in such counting experiments is the Maximum-Likelihood-Method which will be presented in the following chapter. Subsequently, the method is put in context of IceCube(-Gen2) directional reconstructions for cascade events.

4.1 Maximum-Likelihood-Estimation

The **M**aximum-**L**ikelihood-Method[1] (**ML**-Method) is a technique to estimate parameters[2] of a physical hypothesis or model for given uncorrelated data [19].
This estimation builds up on the *likelihood* (function) $\mathcal{L}$. $\mathcal{L}$ is a **p**robability **d**ensity **f**unction (**PDF**), evaluated for the data x, depending on the parameters θ and with respect to an underlying physical hypothesis. This function is maximized in order to estimate the parameters θ [13].
The fruition of the ML-Method depends crucially on the model that describes the examined issue and not only allows a comparison of different hypothesis but also requires competition between them to identify the best fitting parameters. Assuming a physical model is described by the PDF f, then, the likelihood $\mathcal{L}$ can be written for identical and independent data events as a product of f, evaluated at the data points x_i:

$$\mathcal{L}(\theta; x) = \prod_i f(x_i; \theta) \tag{4.1}$$

[19]. Since the values of $\mathcal{L}$ can be very small and to avoid possible numeric issues, the logarithmic value of $\mathcal{L}$ is often used. This is justified by the monotonic behaviour of the logarithm which maintains the extrema of an arbitrary function [13]. Moreover, in practice, the negative logarithmic likelihood is minimized to obtain the maximum of $\mathcal{L}$ [19].
In this thesis, two different approaches for the likelihood function in counting experiments are used. Both can be obtained by modifying the general formulation in eq. (4.1) as will be argued in the following.

[1] also referred to as **M**aximum-**L**ikelihood-**E**stimation (**MLE**)
[2] e.g. direction, energy or vertex position of an incoming neutrino in the case of IceCube

A standard continuous (unbinned) likelihood function, like the one just mentioned in eq. (4.1), can be provided with more information by taking the number N of observed events into account. Therefore, besides the information about the shape, new information about the normalization is added to the likelihood. This can be realized by multiplication with an overall Poisson factor:

$$\frac{e^{-\lambda_{tot}} \cdot \lambda_{tot}^{N}}{N!} \cdot \prod_{i=1}^{N} f\left(x_i; \theta\right) \tag{4.2}$$

where λ_{tot} denotes the total number of expected events [19].
Likelihoods in general, extended with an factor that includes the normalization are called „extended likelihood“ functions [5]. Therefore, the function in eq. (4.2) is referred to as the „**extended unbinned likelihood**“ function.
The second form of the likelihood function used in this thesis can be obtained from eq. (4.2) by transforming the PDF $f\left(x_i; \theta\right)$ into a version with discrete bins (binned) under consideration of the normalization which leads to:

$$\prod_{i=1}^{N_{bins}} \frac{e^{-\lambda_i} \cdot \lambda_i^{k_i}}{k_i!} \tag{4.3}$$

with the number of bins N_{bins}, the observed number of events in a bin k_i and the expected number of events in every bin λ_i. This approach is known as „**Poisson likelihood**“ [19].
If, subsequently, the number of bins is set $N_{bins} = 1$ the introduced likelihood loses its time dependency and the resulting function only depends on the normalization.
The Poisson likelihood and the extended unbinned likelihood are the formulations of interest in this thesis. From the these two likelihoods the latter holds more information than the first, and is therefore more sensitive. This higher amount of information is explained by the circumstance that the latter depends on the „binned approximation“ of a PDF, one bin per DOM, instead of the continuous version [19].

Error estimation on parameters

To judge the validity of estimated parameters in the ML-Method an error estimation is mandatory. A possible way to obtain such an error on a parameter is to determine the so called $n\%$ confidence interval. This interval contains the best estimate of a parameter in $n\%$ of an infinite amount of pseudo-experiments [19].
To obtain a $n\%$ confidence interval[3] in the context of MLE one can do a **likelihood profile scan** as introduced by [41] for directional muon track reconstructions. Here, the directional parameters are varied around the maximum of the likelihood function while all other parameters are set to their best-fit-estimate. This variation takes place in a rotated coordinate system where the directional parameters can be seen as euclidean. Parameters in relation to this rotated coordinate system will be equipped for the remainder of this

[3] or confidence ellipse in the case of 2 degrees of freedom

thesis with a „d“ prefix (e.g. $\varphi \rightarrow \mathrm{d}\varphi$). The shape of the likelihood function for large sample sizes near the maximum is approximately Gaussian. Therefore, a paraboloid is analytically fitted to the likelihood „scan“ where the involved fit parameters not only determine the form of the fitted paraboloid but also can be used to define a 1σ confidence ellipse, so that an error on the parameters can be estimated. The boundaries of the confidence interval correspond to a specific likelihood value which can be obtained from the considerations in section 6.1.

4.2 Directional reconstructions for cascade events in IceCube

Cascade event reconstructions in IceCube require to introduce the concept of „**time residual PDF**“s. This kind of PDF indicates the probability for Cherenkov photons to arrive at a DOM as a function of the time, starting at the first moment light can causally arrive at the module. The underlying physics hypothesis for the time residual PDF considers e.g. position and energy loss processes of the cascade as well as the propagation of photons in the antarctic ice [19],[22].
The PDF is evaluated for every DOM in the detection array depending on vertex position, energy and direction of the neutrino event. A resulting cascade is assumed as point-like in the used reconstructions, justified by the small cascade lengths in proportion to the spacing of the IceCube(-Gen2) strings. Therefore, the overall likelihood L which has to be maximized in order to obtain the parameters θ that describe the final reconstructed event is acquired by multiplication of the likelihood functions $\mathcal{L}_i$ in every single DOM:

$$L(\theta) = \prod_{i=1}^{\mathrm{N_{DOM}}} \mathcal{L}_i(\theta) \tag{4.4}$$

[19]. In this thesis, $\mathcal{L}_i$ is given by eqs. (4.2) and (4.3).
The direction Ψ of an neutrino event is defined by its azimuth angle φ and zenith angle ϑ on the sky. To put the quality of a directional reconstruction into perspective it's necessary to compare the **reconstructed direction** Ψ_{rec} with the **true direction** Ψ_{true}. The relevant physical quantity hereby is the **angular error** $\Delta\Psi$ between reconstruction and truth. $\Delta\Psi$ indicates the angular distance between two points on a sphere, and is thus also called the „**true error**“ of the reconstructed event. It can be computed via:

$$\cos(\Delta\Psi) = \cos(\theta_{\mathrm{true}})\cos(\theta_{\mathrm{rec}}) + \sin(\theta_{\mathrm{true}})\sin(\theta_{\mathrm{true}})\cos(\varphi_{\mathrm{true}} - \varphi_{\mathrm{rec}}). \tag{4.5}$$

At the end of section 4.1 it was explained in which manner an error estimate on reconstructed directional parameters can be obtained. The confidence ellipse determined by this method is characterized by its major and minor axis σ_1 & σ_2. These two errors can be averaged to receive the so called „paraboloid error“

$$\sigma = \sqrt{\frac{\sigma_1^2 \cdot \sigma_2^2}{2}} \tag{4.6}$$

which can be used to define the so called „**pull**“ $\frac{\Delta\Psi}{\sigma}$. The pull is used as a crosscheck for reconstruction methods and the median of it is expected to be constant over event energy for good reconstructions. The ideal value of the pull is roughly 1.177. This resolves from the considerations that σ corresponds to a 39% quantile of a two dimensional gauss while Ψ on average specifies the 50% quantile. The latter is by a factor of 1.177 larger than the first one [19].

5 Dataset & Simulation

The data which was used for the purpose of this thesis is the Monte-Carlo simulated „Dataset 20030“. It consists solely of ν_e events in a neutrino energy range of 10 – 10^5 TeV with a spectral index of -1.4. In addition to that the dataset is based on a assumed spacing of 240 m between the Gen2 strings [34].
The Dataset 20030 also contains MCPE (**m**onte **c**arlo **p**hoto **e**lectron) level pulses where merely photon creation, propagation and their detection in the PMTs (including quantum efficiency and wavelength acceptance) of a DOM is simulated [30]. This allows studies without DOM-related effects. Furthermore, further processed pulses which represent **realistic light pulses** were contained in the dataset. This procession includes the application of „DetectorSim“ on the data to get the response of the PMTs in the DOMs to the light [27]. Moreover, thermal and nonthermal noise, produced by decays in PMTs and DOM glass and subsequent scintillation, in IceCube is necessary and realized via the „Vuvuzela“ application [29],[31]. Lastly, a „BaseProc“ module needs to be applied to the data which among other first reconstruction steps calibrates waveforms and provides the realistic cascade light pulses in a for the utilized reconstructions necessary form [28]. In this context,„realistic“ means that the extension of a cascade with its secondary particles and the propagation of the emerging photons is considered.

5.1 Event selection

An energy selection and further cuts were applied to the dataset in order to gain a sample with 100 Gen2 events in each of the six half decades in the neutrino energy range from 10 TeV – 10 PeV, leading to an overall number of 600 events. After the energy selection, two cuts were applied to obtain an event sample that contains solely Gen2 events: first, an event should trigger photon hits in no more than 50 DOMs of the IceCube In-Ice Array. This number can't be set to zero since the in IceCube generated noise itself produces hits in DOMs which don't have their origin in a neutrino event. The concrete number of 50 is motivated by the investigation of the histogram with the number of IceCube DOMs triggered,„$n_{channels}$“, which can be found in fig. 5.1. Normally, the first peak contains all events where only noise in the IceCube In-Ice Array is detected. For this dataset, this isn't the case due to faulty noise generation which leads to a higher number of noise hits than usual. Therefore, it was necessary to apply a generous cut at $n_{channels} = 50$ in order to effectively remove all standard IceCube events. The last applied cut was to require

triggered photon hits in at least four Gen2 strings $n_{strings,Gen2}$. This was done to get only events which don't lie at the edge of the detector and deploy a reasonable amount of photons in the Gen2 part for event reconstructions. The corresponding histogram with the number of Gen2 strings triggered by an event in the dataset is displayed in fig. 5.2. An overview of the event selection can be found in table 5.1.

number of cut	applied cut
#1	energy selection
#2	$n_{channels}$ in IC-86 ≤ 50
#3	$n_{strings,Gen2} \geq 4$

Table 5.1: Applied cuts to the dataset. $n_{channels}$ in IC-86 denotes the number of standard IceCube DOMs triggered by photons of an event while $n_{strings,Gen2}$ stands for the triggered number of Gen2 strings.

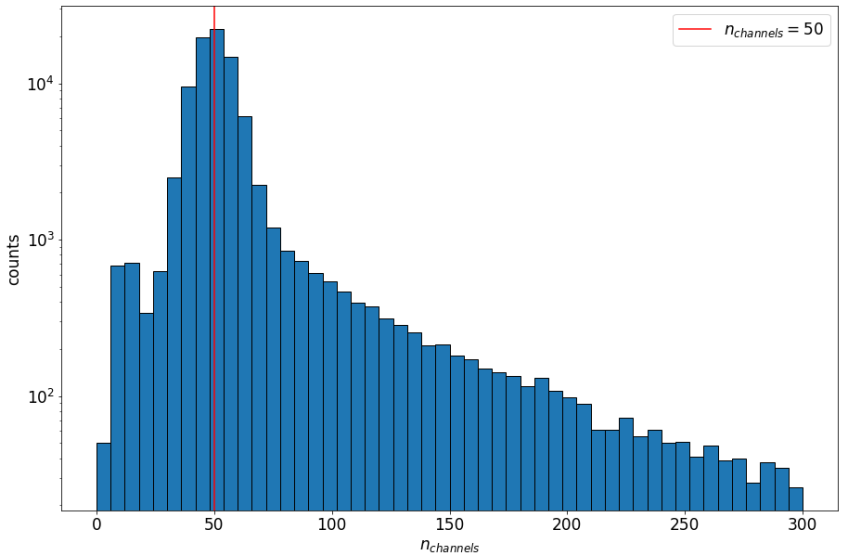

Figure 5.1: Distribution of IC-86 DOMs triggered by photons $n_{channels}$ for the pre-cuts dataset, limited to the range of 0 – 300. Applied cut $n_{channels} = 50$ displayed by red vertical line.

The post-cuts histograms with the energy spectra for each half decade can be found in fig. 5.3 while the ones for the number of strings hit in Gen2 as well as the number of DOMs hit in IceCube can be found in the figs. 5.4 and 5.5.

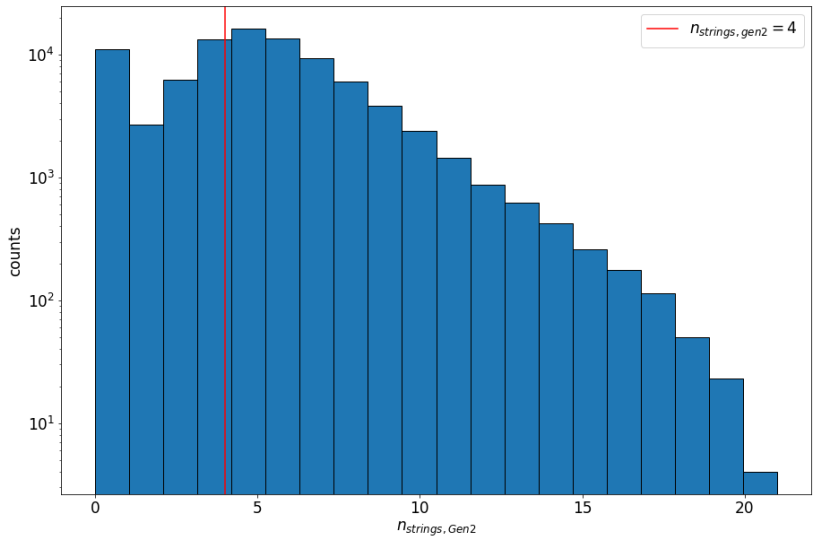

Figure 5.2: Distribution of number of Gen2 strings triggered by photons $n_{strings,Gen2}$ for the pre-cuts dataset. Applied cut $n_{strings,Gen2} = 4$ displayed by red vertical line.

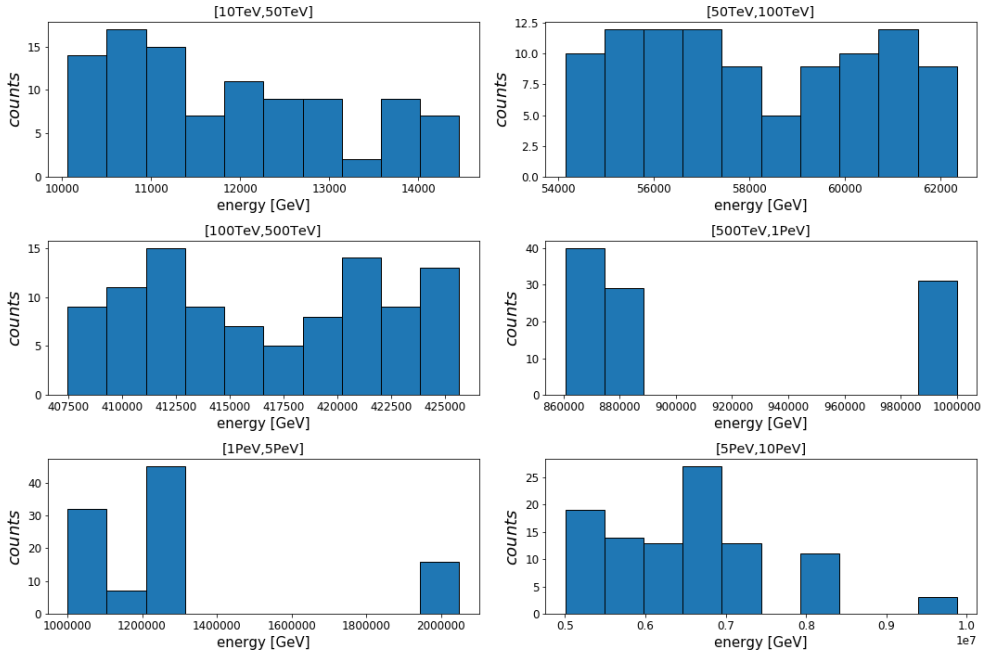

Figure 5.3: Neutrino energy distribution for each of the six half decades in the post-cuts dataset.

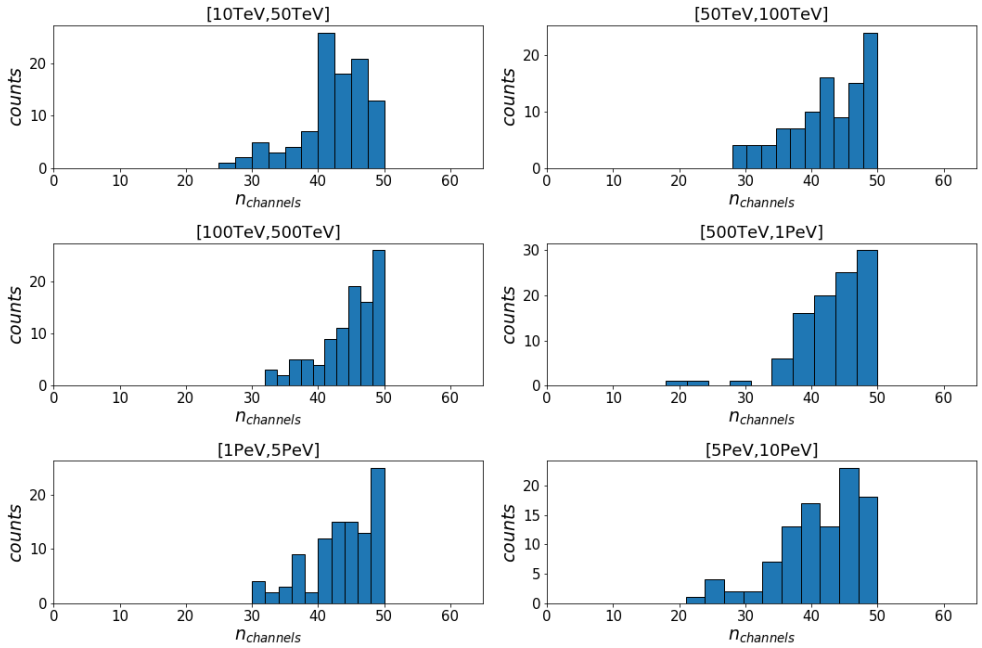

Figure 5.4: Distribution of the number of IC-86 DOMs triggered by photons $n_{channels}$ for each of the six half energy decades in the post-cuts dataset.

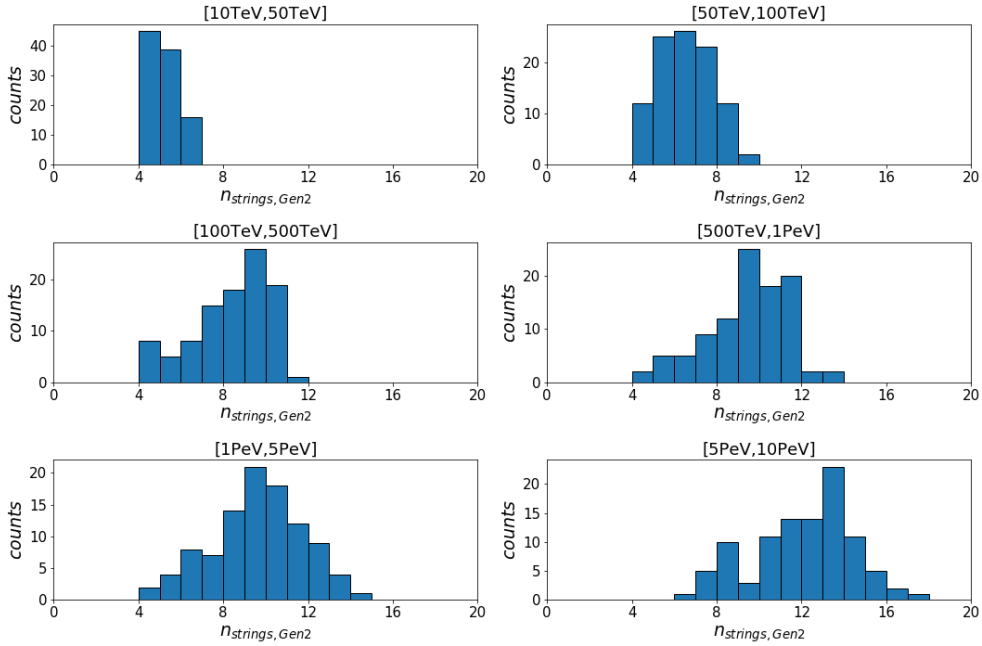

Figure 5.5: Distribution of the number of Gen2 strings triggered by photons $n_{strings,Gen2}$ for each of the six half energy decades in the post-cuts dataset.

5.2 Generation of idealized light pulses

The light pulses in the dataset 20030 were simulated for mDOMs. As a cross check and to simulate light for the PDOM, a simple way to generate **idealized light pulses** was used. This technique is explained in following.
In order to understand the principle of this method it is necessary to introduce the concept of spline tables. As mentioned in section 4.2, the time residual PDF indicates the probability for Cherenkov photons to arrive over time. In reconstructions this PDF is evaluated for every **o**ptical **m**odule (**OM**) to maximize the likelihood, and therefore determine the parameters of an event. In practice, the time residual PDF isn't computed during the maximization process but beforehand for all kind of different event parameter combinations, like for instance vertex position or shower energy. Spline functions are fitted to these discrete evaluations of the likelihood and saved in tables, the so called spline tables.
If the cascade event properties are known, as in the used dataset, the spline tables provide the mean amplitude of the corresponding photon hit distribution. In this context, the cascade is considered point-like. The retrieved amplitude is used to size up the number of hits in an OM with respect to a Poisson distribution.
Furthermore, one can obtain the time residual PDFs for every OM from the spline tables. The estimated number of hits in an OM is subsequently utilized to evaluate the time residual PDF, and thus to sample the light pulses in an OM.
To take into account that the effective photo cathode area of the mDOM is roughly twice as big as the one of the PDOM, compare section 3.3.1, the mean amplitude of the photon hit distribution for the PDOMs was scaled with a factor of 2.2.

6 Results

The following chapter presents the results of the directional reconstructions for the cascade dataset 20030.
First, likelihood scans for some example events as well as the angular error and pull medians of the realistic pulses will be shown and discussed as a „proof of concept“.

6.1 Proof of concept

In order to proof that the reconstruction concept operates as expected four different events in the regime of $\approx 10\,\mathrm{TeV}$, compare table 6.1, were reconstructed for the mDOM with the Poisson and extended unbinned likelihood hypothesis (see chapter 4). These reconstructions were performed on idealized light pulses and on realistic light pulses, see chapter 5. The properties of the event reconstructions, namely the angular error $\Delta\Psi$ and the number of minimization steps, for the idealized and the realistic pulses can be found also in table 6.1.

Moreover, likelihood scans as introduced in section 4.1 were created for the events which are displayed in figs. 6.1 and 6.2 for the idealized pulses and in figs. 6.3 and 6.4 for the realistic pulses. The thereby plotted test statistic is defined by the quantity

$$\lambda = -2 \cdot log\left(\frac{\mathcal{L}}{\mathcal{L}_0}\right) = -2\left(log\left(\mathcal{L}\right) - log\left(\mathcal{L}_0\right)\right) \tag{6.1}$$

where $\mathcal{L}_0$ is the maximized likelihood function dependent on all its m parameters, including direction, vertex position, energy and dependend on the used hypothesis time. Whereas $\mathcal{L}$ in the numerator is set fixed in b parameters which maximize $\mathcal{L}_0$, leaving $k = m - b$ variable parameters. In this context of directional cascade reconstructions, k is given by the two directional parameters φ & ϑ, respectively $\mathrm{d}\varphi$ & $\mathrm{d}\vartheta$[1]. This test statistic is an approximation[2] of the usually used test statistic where $\mathcal{L}$ is maxmimized in the b parameters for every examined combination of the k parameters. According to Wilk's theorem λ converges to the χ^2-distribution with k degrees of freedom in the case of high statistics. This can be used to obtain the in the plots stated 50% and 95% **c**onfidence **i**ntervals (**CI**) [19].
Furthermore, the minimization steps are illustrated in the plots. Hereby, the coordinate

[1] $\mathrm{d}\varphi = \varphi_{\mathrm{true}} - \varphi$, $\mathrm{d}\vartheta = \vartheta_{\mathrm{true}} - \vartheta$
[2] Approximation because the other parameters are fixed

system of the reconstruction is orientated such that the start point of each minimization lies at $\mathrm{d}\varphi = 0^\circ$ & $\mathrm{d}\vartheta = 0^\circ$ and equals the true direction of the neutrino event. The end point of the minimization, respectively the found minimum, can be found in the middle of a scan. In order to allow a comparison between the scans, the displayed test statistic was compressed in each plot to a scale beginning at the found minimum which is zero due to the construction of λ in eq. (6.1), leading up to a value of ten.
In general, the plotted likelihood scans show largely smooth behavior of the likelihood functions which is desirable since it provides a robustness for the localization process of the minima [44].
The scans for the realistic pulses sometimes seem to have narrower minima than the

(a) **idealized pulses**

	energy [GeV]	$\Delta\Psi_{\text{Poisson}}$ [deg]	$\Delta\Psi_{\text{unbinned}}$ [deg]	n_{Poisson}	n_{unbinned}
event 0	10675.8	63.68	58.97	314	1173
event 1	10646.1	3.91	16.13	292	505
event 2	10545.9	1.48	48.80	282	1017
event 3	10145.8	12.64	54.96	380	351

(b) **realistic pulses**

	energy [GeV]	$\Delta\Psi_{\text{Poisson}}$ [deg]	$\Delta\Psi_{\text{unbinned}}$ [deg]	n_{Poisson}	n_{unbinned}
event 0	10675.8	8.41	17.98	200	253
event 1	10646.1	30.37	9.16	329	571
event 2	10545.9	12.06	254	333	
event 3	10145.8	4.33	178	287	

Table 6.1: Reconstruction properties of the four example events where $\Delta\Psi_{\text{Poisson}}$ & $\Delta\Psi_{\text{unbinned}}$ stand for the angular error while n_{Poisson} & n_{unbinned} denote the number of minimization steps of the Poisson and extended unbinned likelihood hypothesis.

idealized pulses.
However, it has to be mentioned that the shown likelihood scans display merely a two dimensional projection of a higher dimensional likelihood function which also depends on event energy and vertex position of the neutrino interaction. This aspect justifies that the exact contour of the minima in the scans shouldn't be overvalued in terms of judging the quality of a reconstruction.

Comparing the true error of the Poisson likelihood reconstructions $\Delta\Psi_{\text{Poisson}}$ with the one from the extended unbinned likelihood reconstructions $\Delta\Psi_{\text{unbinned}}$ leads to the finding

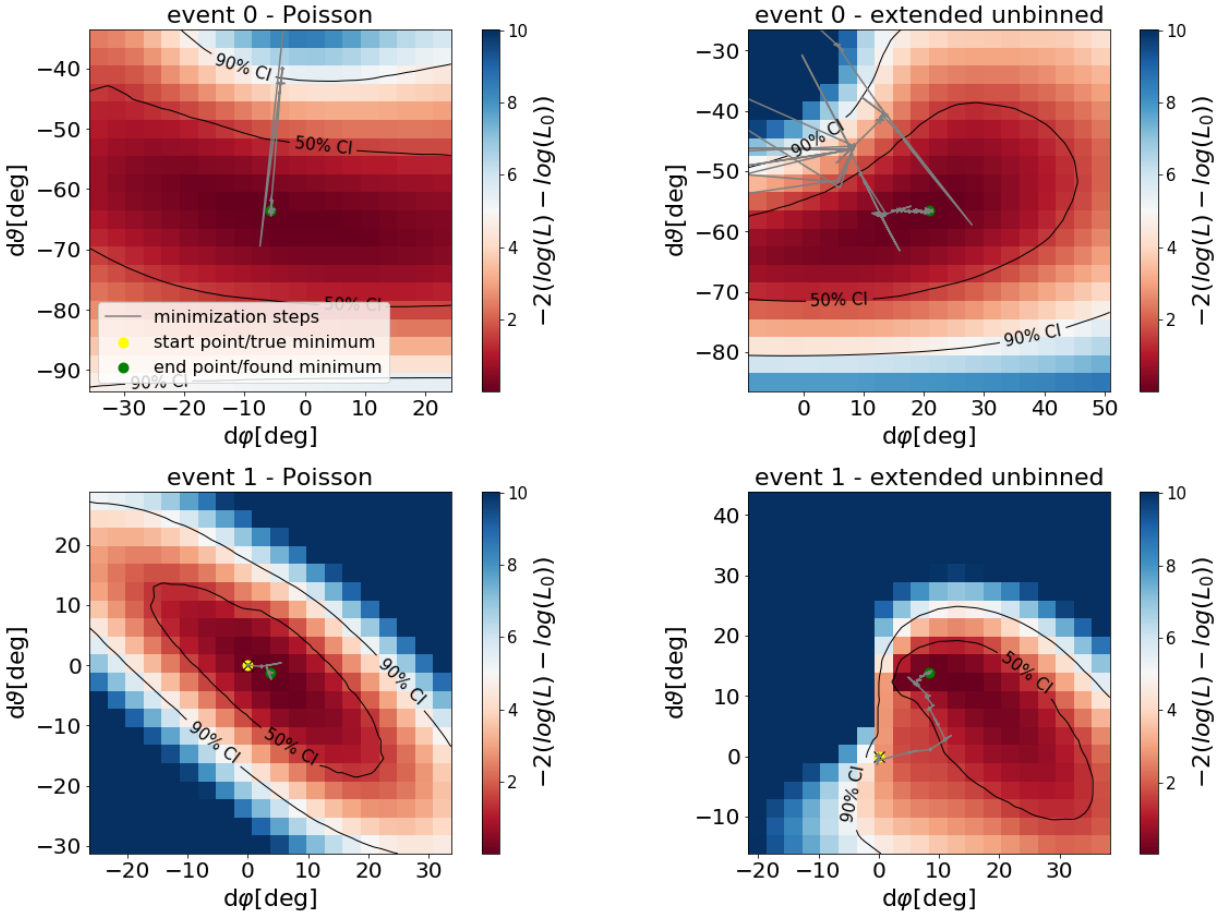

Figure 6.1: Likelihood scans for the directional parameters $\mathrm{d}\varphi$ & $\mathrm{d}\vartheta$ for events 0 & 1 of the event reconstructions with the Poisson (**left**) and extended unbinned hypotheses (**right**), each based on the **idealized pulses**. The plotted test statistic $\lambda = -2\,(log\,(\mathcal{L}) - log\,(\mathcal{L}_0))$ is compressed, beginning at the minimum value λ_{min} and leading up to $\lambda_{\mathrm{min}} + 10$. Furthermore, the minimization steps (grey) with its start (yellow) and end point (green) are displayed. Additionally, the 50% & 90% **c**onfidence **i**ntervals (**CI**) are plotted (black).

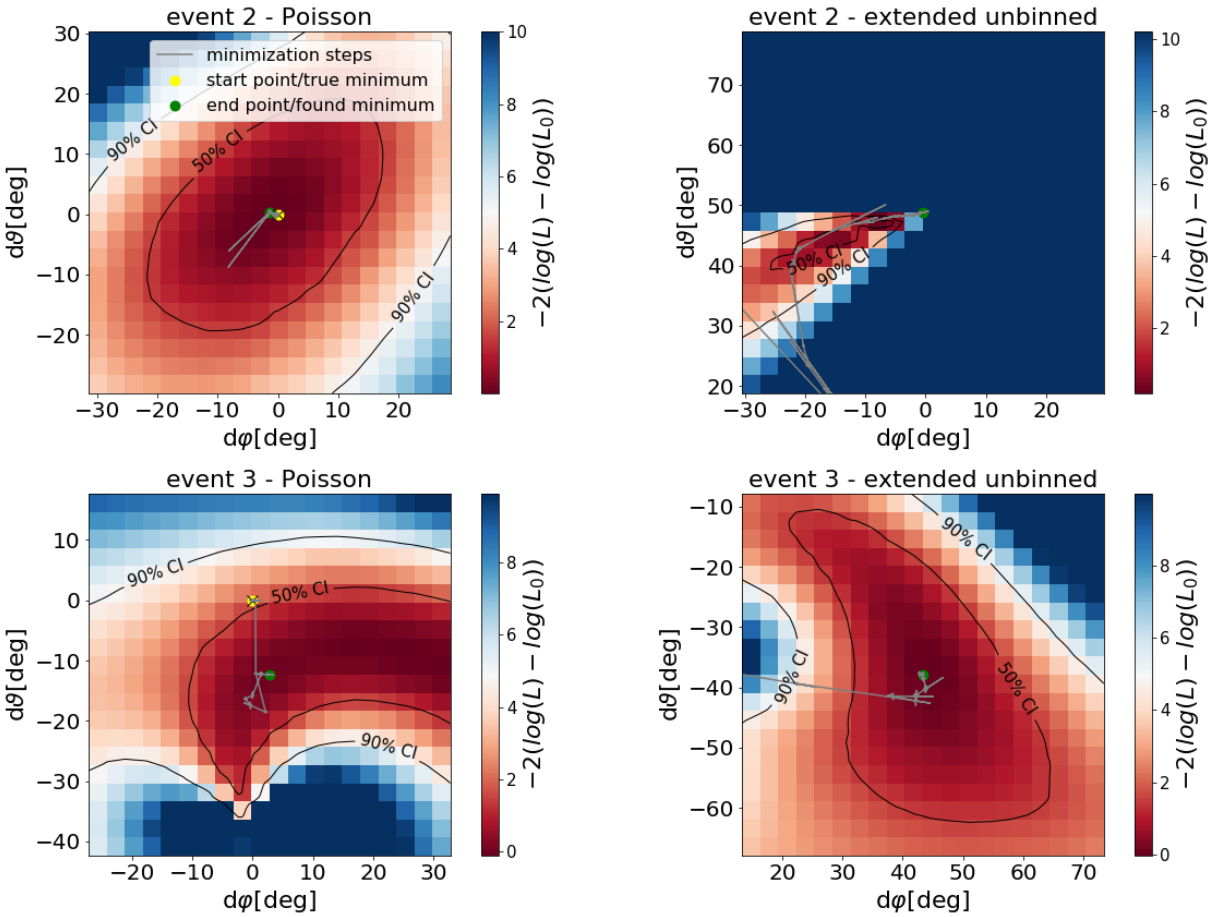

Figure 6.2: Likelihood scans for the directional parameters $\mathrm{d}\varphi$ & $\mathrm{d}\vartheta$ for events 2 & 3 of the event reconstructions with the Poisson (**left**) and extended unbinned hypotheses (**right**), each based on the **idealized pulses**. The plotted test statistic $\lambda = -2\left(log\left(\mathcal{L}\right) - log\left(\mathcal{L}_0\right)\right)$ is compressed, beginning at the minimum value λ_{min} and leading up to $\lambda_{\mathrm{min}} + 10$. Furthermore, the minimization steps (grey) with its start (yellow) and end point (green) are displayed. Additionally, the 50% & 90% **c**onfidence **i**ntervals (**CI**) are plotted (black).

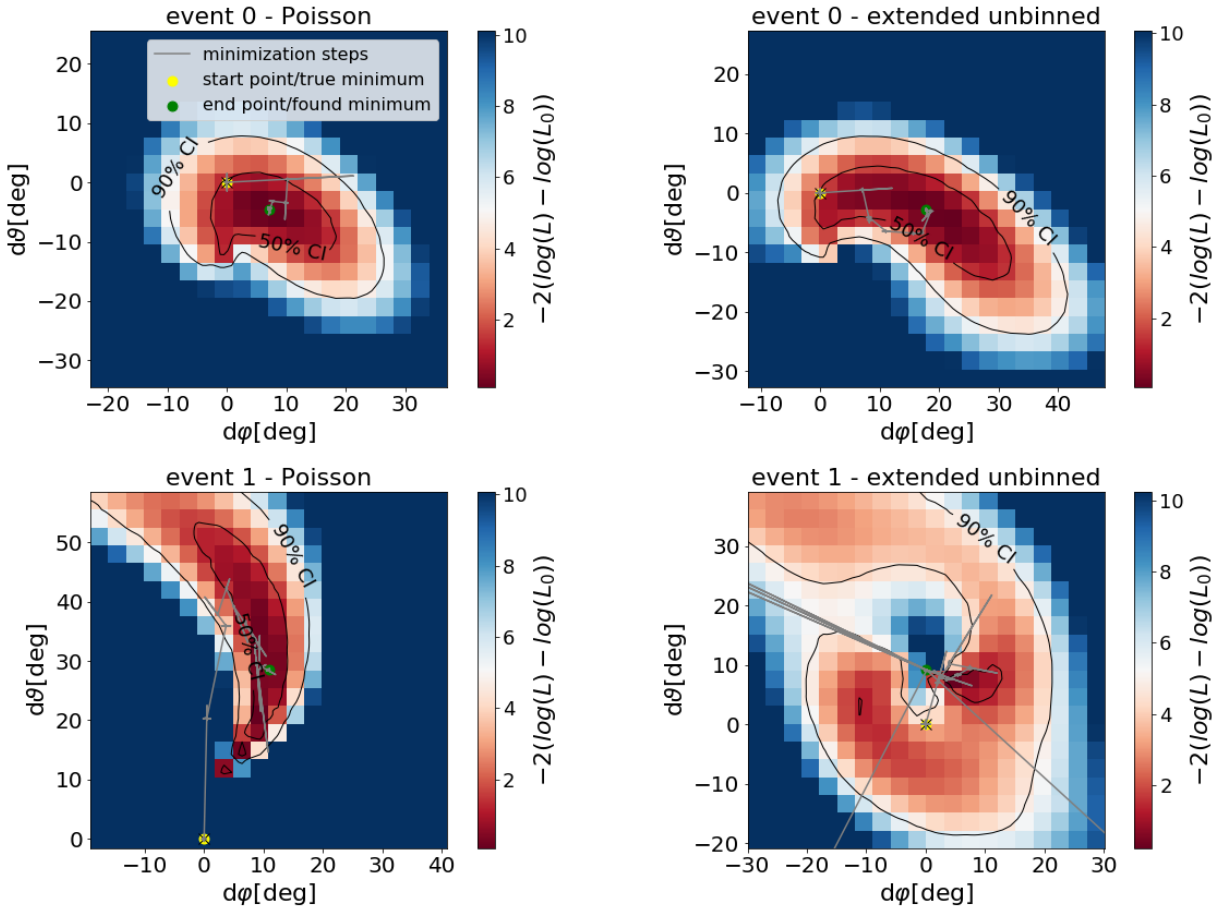

Figure 6.3: Likelihood scans for the directional parameters $d\varphi$ & $d\vartheta$ for events 0 & 1 of the event reconstructions with the Poisson (**left**) and extended unbinned hypotheses (**right**), each based on the **realistic pulses**. The plotted test statistic $\lambda = -2\,(log\,(\mathcal{L}) - log\,(\mathcal{L}_0))$ is compressed, beginning at the minimum value λ_{min} and leading up to $\lambda_{\text{min}} + 10$. Furthermore, the minimization steps (grey) with its start (yellow) and end point (green) are displayed. Additionally, the 50% & 90% **c**onfidence **i**ntervals (**CI**) are plotted (black).

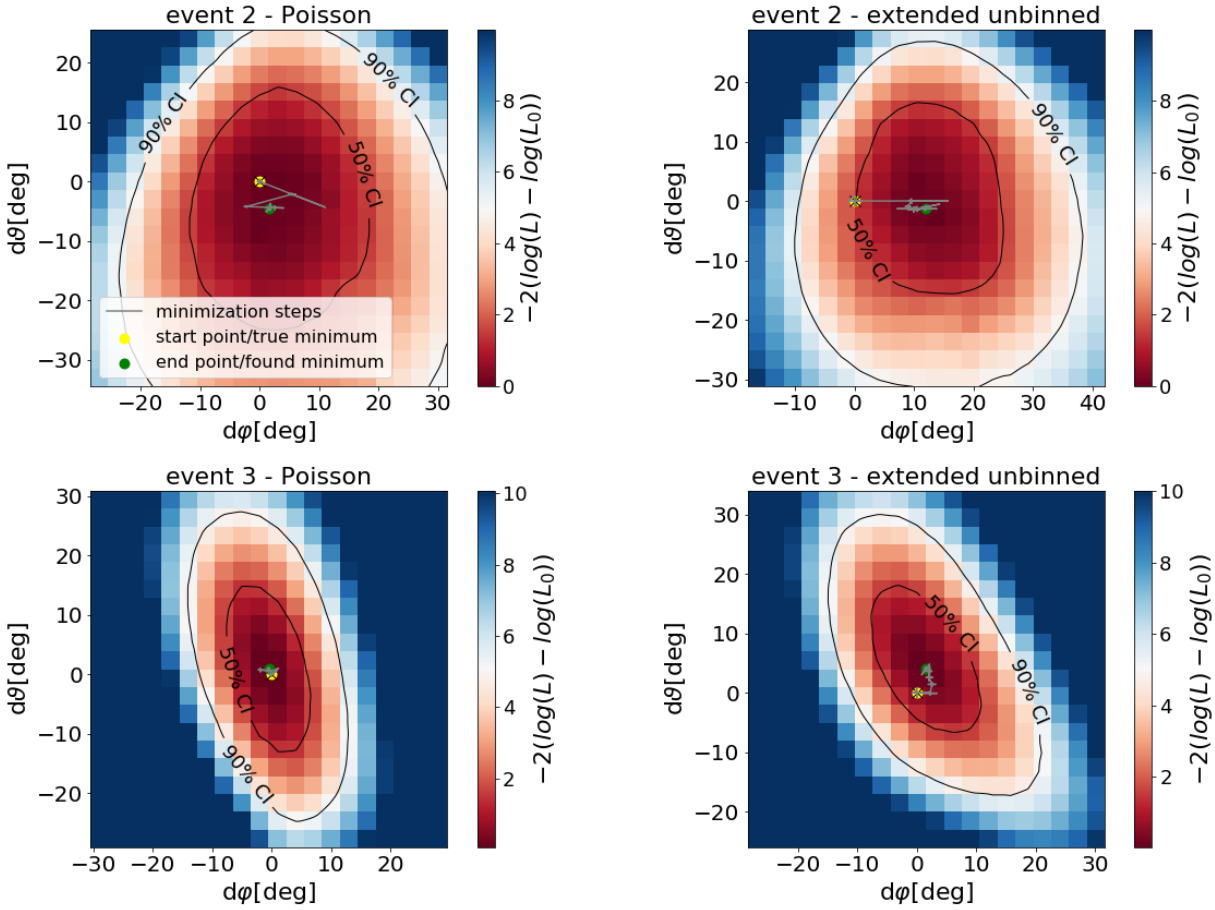

Figure 6.4: Likelihood scans for the directional parameters $d\varphi$ & $d\vartheta$ for events 2 & 3 of the event reconstructions with the Poisson (**left**) and extended unbinned hypotheses (**right**), each based on the **realistic pulses**. The plotted test statistic $\lambda = -2\,(log\,(\mathcal{L}) - log\,(\mathcal{L}_0))$ is compressed, beginning at the minimum value λ_{min} and leading up to $\lambda_{\text{min}} + 10$. Furthermore, the minimization steps (grey) with its start (yellow) and end point (green) are displayed. Additionally, the 50% & 90% **c**onfidence **i**ntervals (**CI**) are plotted (black).

that $\Delta\Psi_{\text{Poisson}} < \Delta\Psi_{\text{unbinned}}$. This is against the expectation that an unbinned likelihood should yield better reconstruction results than a binned approach with only one bin due to the higher amount of information which a continuous construction inherits. A potential reason for this could be that the extended unbinned hypotheses leads to a complex likelihood function with several local minima, the used minimization algorithm gets stuck in one of them, and therefore the global minimum isn't found. Investigations in this context are presented in section 6.1.1. Furthermore, it has to be recognized that the reconstruction are based on the assumption of a point-like cascade without extension. Thus, the physical hypothesis is technically an approximation, and therefore can lead to wrong results for the realistic pulses.
In order to really test a reconstruction method a sufficient number of reconstructed events over a large energy range is necessary. This requirement is fulfilled by reconstructing all 600 events of the dataset.
As mentioned before, the most important parameter of interest in directional reconstructions is the true error $\Delta\Psi$ and its behavior over energy. To investigate it the energy medians for each of the half decades which are provided by the dataset were computed and plotted against the corresponding medians of $\Delta\Psi$. In addition, the pull $\frac{\Delta\Psi}{\sigma}$, where σ denotes the paraboloid error, was examined by also plotting the medians of the pull over the energy medians.
$\Delta\Psi$ is expected to decrease for higher energies as the number of photons arriving at the DOMs rises. Therefore, the amount of available information increases which leads to more convenient likelihood functions, and thus better reconstructions. As stated at the end of section 4.2, the pull is expected to be constant over energy and has a ideal value of 1.177.
The results of the Poisson reconstructions based on the realistic pulses are shown in fig. 6.5 and discussed in the following. $\Delta\Psi$ decreases from the first energy „bin“ to the second one but after that a kind of „oscillating“ behavior of the curve occurs. This isn't compatible with the expectation of a steady decrease of the course. A possible explanation could be the idealizing assumption of the reconstruction that the cascade is point-like, contrary to the approach of the realistic pulses where the expansion of a cascade is taken into account. Since the length of a cascade increases with the energy, the point-like assumption of a cascade gets more and more insufficient. This effect competes with the improvement of a reconstructions with higher energies due to the higher amount of accessible information and could possibly lead to the fluctuating behavior. However, under consideration of the 14% & 86% quantiles of the true errors, see fig. 6.6, it stands out that the fluctuation is probably due to statistic fluctuations. The computed pull also does not fulfill the expectation of a constant behavior over energy since it increases for higher energies. Due to two events in the $1 - 5\,\text{PeV}$ range where the paraboloid error didn't yield a finite value the median of the pull for this energy bin was calculated with 98 instead of 100 events. The low values of $\frac{\Psi}{\sigma}$ in the low energy regime implies a large paraboloid error compared to the true error. As a possible reason for this could be named that the Gaussian approximation in the minimum of the likelihood doesn't apply if the minimum isn't found or the number of data events is too low. Thereby, the paraboloid

fits would yield large errors. For higher energies, the pull exceeds the expected ideal value of 1.177.
The unexpected and in the scope of this thesis irremediable behavior of the true error curve for the realistic pulses lead to the decision to use the idealized pulses for the further course of this thesis as these pulses yield better results as will be presented in section section 6.2.

6.1.1 Investigation of the minimization process

As mentioned before, the worse true error of the extended unbinned likelihood compared to the Poisson likelihood could be due to a minimization issue where only a local minimum is found. Therefore, the used minimizers and possible alternatives are introduced.
The first minimizer to name is „migrad“ of the Python iminuit package which is basically a variable metric algorithm [42]. Variable metric optimizers build up on the Newton-Raphson method and approximate the thereby used inverse of the Hessian matrix [16][38].
Another used minimizer is provided by the Python package „emcee“ which is based on a **M**arkov **c**hain **M**onte **C**arlo (**MCMC**) method. MCMC optimization algorithms offer the possibility to leave local minima since their minimization steps usually have a non-zero probability to accept values which are less extreme than the previous ones. Therefore, there is a chance for the optimizer to leave a found local minimum [17][21].
A third alternative minimizer is given in „BOBYQA“ of the NLopt package. BOBYQA is a derivative-free optimizer for bound constraint optimization problems [12][45].
As a preliminary remark, all of the subsequent minimization procedures for the different likelihoods follow a pure energy fit to reduce the actual minimization steps.
The minimization for the Poisson likelihood in the mDOM case of the idealized pulses as well as the previously presented realistic pulses was done with 500 steps of migrad followed by 800 steps of emcee. Steps stand in this context for the approximate maximal number of minimization steps until the algorithms stop which normally results in less actual optimization steps as presented in table 6.1. The Poisson likelihood based on the idealized pulses for the PDOM and the extended unbinned approaches for PDOM & mDOM, again performed on the idealized pulses, were each minimized with 2000 steps of migrad.
In order to check if the minimization algorithm gets stuck in local minima during the optimization process of the extended unbinned likelihood function events 2 & 3 were each reconstructed on the idealized pulses with two different minimization procedures. These events were chosen since they provide the largest discrepancy between $\Delta\Psi_{\text{unbinned}}$ and $\Delta\Psi_{\text{Poisson}}$ of the four test events, compare table 6.1.
The first attempt was made by using three times 2000 steps of migrad and 800 steps of BOBYQA, leading to a total amount of six[3] minimizers in a row. The resulting likelihood scans are plotted in fig. 6.7 together with the corresponding scans from fig. 6.2. True error and number of actual minimization steps are entered in table 6.2a. The new minimization

[3] respectively seven minimizers if one counts the energyfit in the beginning

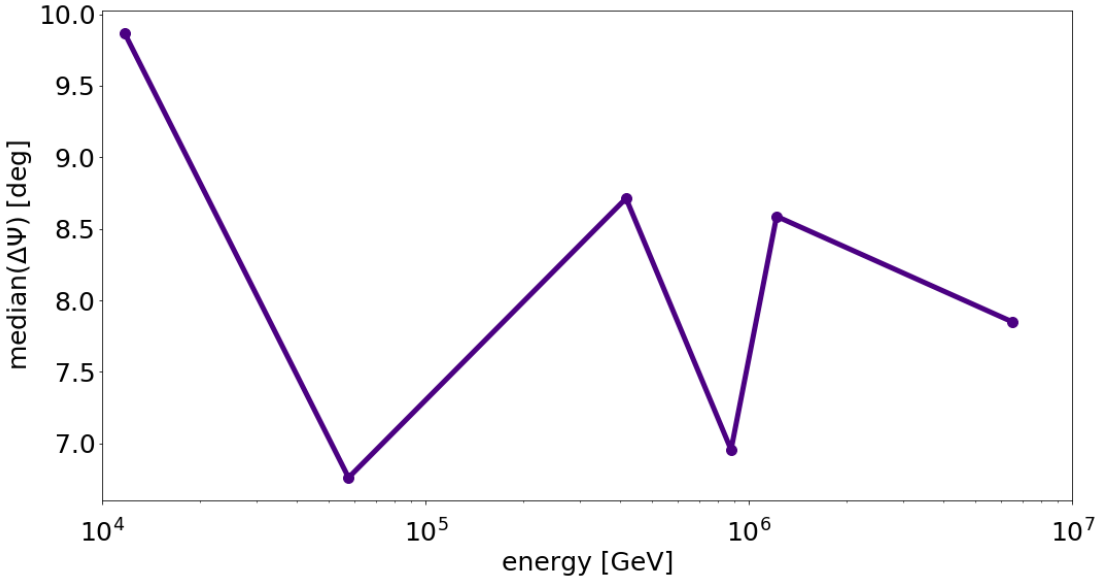

(a)

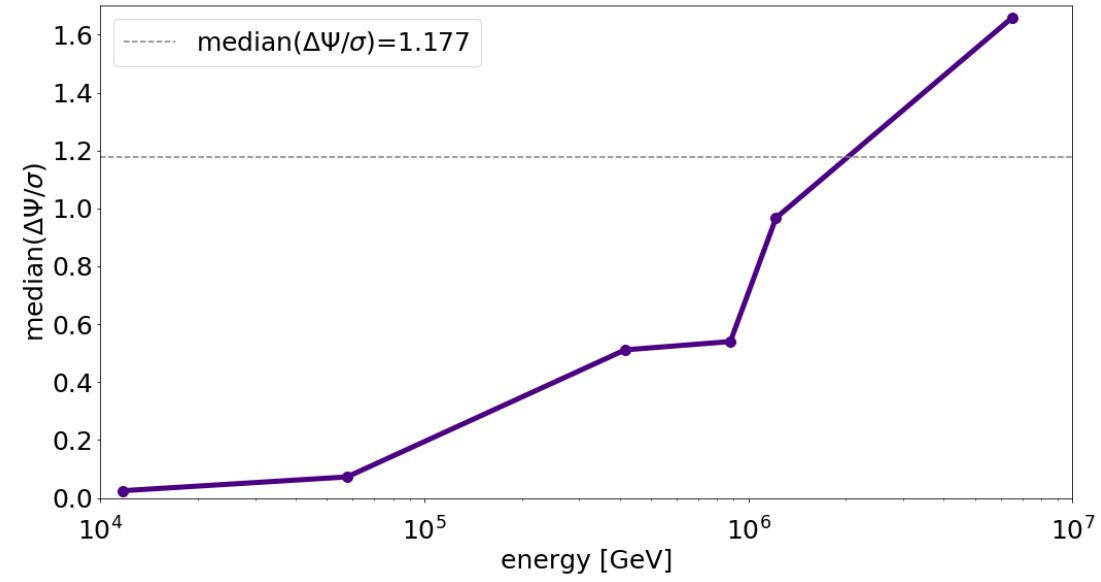

(b)

Figure 6.5: (**a**) True error $\Delta\Psi$ & (**b**) pull $\frac{\Delta\Psi}{\sigma}$ over event energy for the **mDOM** Poisson reconstruction with the realistic pulses. Ideal pull median value of 1.177 is plotted in **grey**.

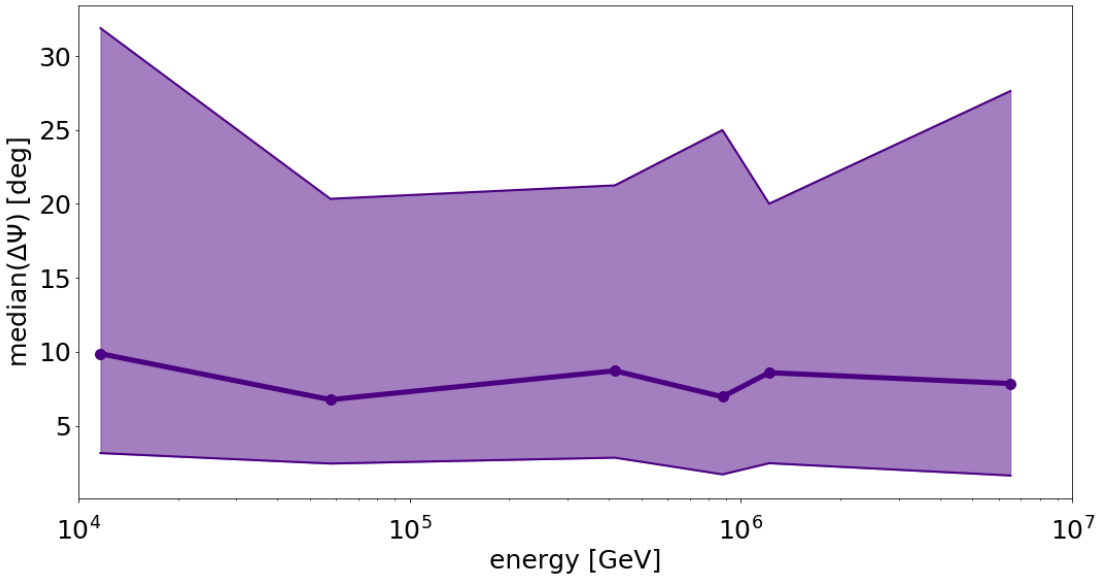

Figure 6.6: True error median $\Delta\Psi$ with 14% and 86% quantiles, displayed by **purple** colored area, over event energy for the mDOM Poisson reconstruction with the realistic pulses.

process compared to the regular minimization shows effectively no difference. Only the plotted minimization steps and the actual number of minimization steps differ. They imply that the minimizer methods find these possibly local minima early and stay in them for the rest of the process.

As a second effort, the two events were reconstructed with 2000 emcee and 2000 migrad

	$\Delta\Psi_{\text{unbinned}}$ [deg]	n_{unbinned}
event 2	48.80	1561
event 3	54.96	789

(a) 3·(migrad 2000 + BOBYQA 800)

	$\Delta\Psi_{\text{unbinned}}$ [deg]	n_{unbinned}
event 2	48.67	2962
event 3	57,60	2513

(b) (emcee 2000 + migrad 2000)

Table 6.2: Reconstruction properties of the example events 2 & 3 where $\Delta\Psi_{\text{unbinned}}$ & n_{unbinned} denote true error and number of minimization steps of the extended unbinned likelihood hypothesis. (**a**) minimization procedure with three times migrad with 2000 and BOBYQA with 800 steps. (**b**) minimization via 2000 steps emcee followed by migrad with 2000 steps.

steps. This approach was used in order to take advantage of the further stated possibility to evade local minima with MCMC based optimizers like emcee. The corresponding likelihood scans are displayed in fig. 6.8 while the reconstruction properties are presented

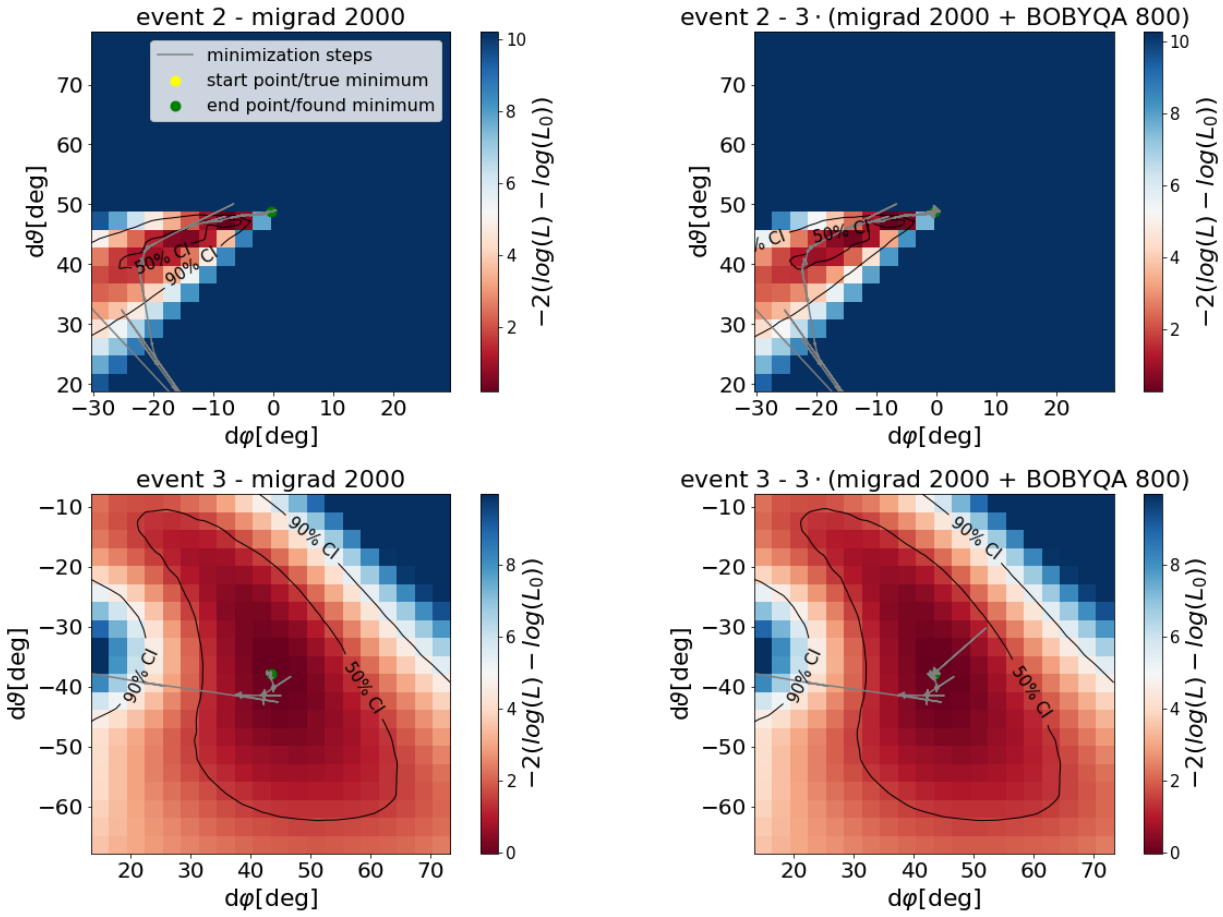

Figure 6.7: Likelihood scans in directional parameters $\mathrm{d}\varphi$ & $\mathrm{d}\vartheta$ for the reconstructions of events 2 & 3 with the extended unbinned hypotheses, based on idealized pulses. Comparison of the minimization procedures between the standard minimization with migrad 2000 (**left**) and the minimization with $3 \cdot$ (**migrad 2000 + BOBYQA 800**) (**right**). The plotted test statistic $\lambda = -2\,(log\,(\mathcal{L}) - log\,(\mathcal{L}_0))$ is compressed, beginning at the minimum value λ_{min} and leading up to $\lambda_{\mathrm{min}} + 10$. Furthermore, the minimization steps (grey) with its start (yellow) and end point (green) are displayed. Additionally, the 50% & 90% **c**onfidence **i**ntervals (**CI**) are plotted (black).

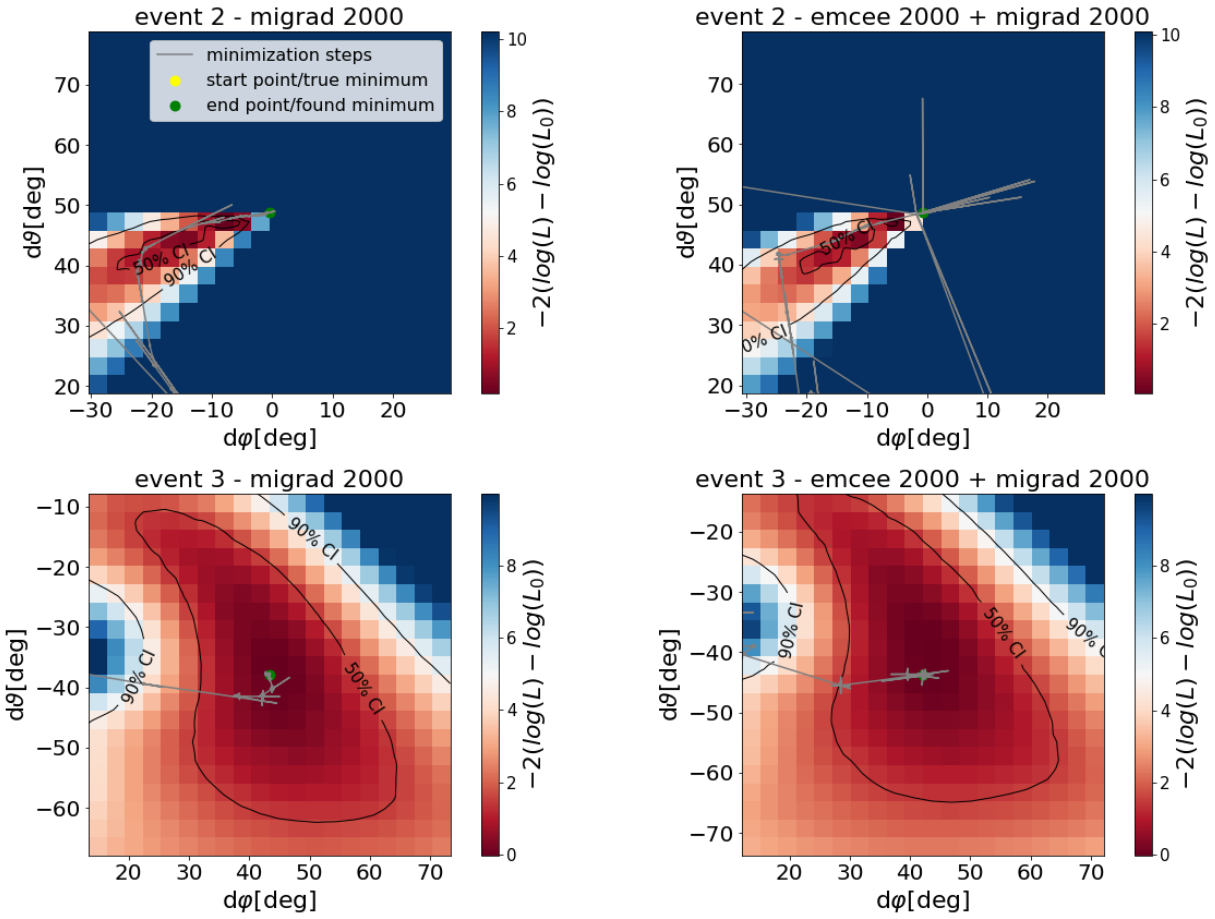

Figure 6.8: Likelihood scans in directional parameters $d\varphi$ & $d\vartheta$ for the reconstructions of events 2 & 3 with the extended unbinned hypotheses, based on idealized pulses. Comparison of the minimization procedures between the standard minimization with migrad 2000 (**left**) and the minimization with (**emcee 2000 + migrad 2000**) (**right**). The plotted test statistic $\lambda = -2\,(log\,(\mathcal{L}) - log\,(\mathcal{L}_0))$ is compressed, beginning at the minimum value λ_{min} and leading up to $\lambda_{\text{min}} + 10$. Furthermore, the minimization steps (grey) with its start (yellow) and end point (green) are displayed. Additionally, the 50% & 90% **c**onfidence **i**ntervals (**CI**) are plotted (black).

in table 6.2b. As in the previous case: apart from the minimization steps and their affiliated higher numbers no significant difference of the reconstructed direction can be observed.
These equal results without improving the angular error lead to the conclusion that the worse true errors of the extended unbinned likelihood compared to the Poisson likelihood probably aren't a consequence of the optimization process but of other unidentified issues with the reconstruction method. Further examination of this problem is therefore necessary in the future.

6.2 Angular error & pull for idealized light pulses

After showing that the principle of the reconstruction works at least on a basic level as expected the results of the reconstruction method for the application on the idealized pulses of the whole dataset are presented and discussed.
The results are presented and compared to their expectations for the PDOM & mDOM individually first and compared to each other afterwards. The true error $\Delta\Psi$ and the pull $\frac{\Delta\Psi}{\sigma}$ are here the quantities of interest.

6.2.1 PDOM

During the reconstruction process of the dataset for the PDOM, a low number of events yielded errors when writing the files, and therefore aren't included in the following. This affected one event of the Poisson likelihood and two events of the extended unbinned likelihood reconstruction. Additionally, two events of the Poisson likelihood produced paraboloid errors with „NaN“ as value which thus couldn't be included in the computation of the pull.
The resulting angular error $\Delta\Psi$ and pull $\frac{\Delta\Psi}{\sigma}$ over energy for both likelihood approaches are displayed in fig. 6.9. $\Delta\Psi$ shows for each of the hypothesis the expected behavior that the true error decreases with increasing energy with the exception of the first two energy bins of the Poisson likelihood reconstruction. Here, an enlargement of the angular error takes place. Moreover, the extended unbinned likelihood exhibits a better angular resolution. This is expected due to the higher amount of information which the extended unbinned likelihood considers. Merely the 10 – 50 TeV bin indicates a slightly better resolution for the Poisson likelihood. This coincides with the observations of the mDOM likelihood scans in the low energy range, see section 6.1. While both hypotheses start with a true error of $\Delta\Psi \sim 16°$ in the lowest energy bin the extended unbinned likelihood improves up to a value of roughly 1.3° whereas the Poisson approach improves only up to approximately 3.3°. The $\Delta\Psi$ median values for the energy bins are displayed in table 6.3.
The pull for both PDOM likelihoods shows neither the prediction of a constant curve nor the expected ideal value of 1.177. Instead, the curves increase with growing energy until they fall off for the higher energies. Furthermore, the pull has throughout smaller values,

especially for the Poisson likelihood hypothesis, which suggests a large paraboloid error σ. An attempt to explain this behavior can be found in section 6.1. Nevertheless, $\frac{\Delta\Psi}{\sigma}$ of the extended unbinned access has for the middle energy bins reasonable values near the expectation of 1.177.

6.2.2 mDOM

Equally to the PDOM reconstructions, some events delivered errors in the writing process of the mDOM reconstruction files. This includes a total of nine events for the Poisson reconstructions and 16 events of the extended unbinned approach. Further, two events which were reconstructed with the extended unbinned likelihood provided „NaN“ values as an outcome for the paraboloid error, and thus had to be dropped for the pull calculation. The corresponding plots for the angular error and the pull are displayed in fig. 6.10.
Overall, the true errors $\Delta\Psi$ of both mDOM reconstruction methods show a decrease with growing energies which corresponds to the previously mentioned expectations. However, for the low energies, the Poisson approach of the reconstruction yields better angular errors, starting with roughly 8.3°, than the extended unbinned approach with approximately 15.0°. As stated before, on the one hand this isn't compatible with the general expectation that the extended unbinned likelihood should yield better angular errors. On the other hand this observation is consistent with the findings of the test event reconstructions in the low energy range for the mDOM (section 6.1) where similar behavior could be observed. For higher energies the curves of the Poisson and the extended unbinned likelihood reconstructions align with a slight advantage for the latter at $< 2°$. An overview of the medians of $\Delta\Psi$ for each energy bin can be found in table 6.3. The pull $\frac{\Delta\Psi}{\sigma}$ of the mDOM reconstructions isn't consistent with the expectations of a constant curve. After an increase in the low energy regime the curve of the extended unbinned pull flattens for higher energies and decreases finally. The Poisson pull shows also an increasing behavior with the energy but then flattens only for the highest displayed energies. The concrete values of $\frac{\Psi}{\sigma}$ for the Poisson likelihood approach are smaller than the ideal value of 1.177, in particular for the lowest energies. The extended unbinned pull values are larger than the just mentioned values of the Poisson pulls and are close to the ideal value of 1.177 for the middle energies but fall off for the lowest and highest investigated energies. As mentioned in the previous sections, the small values of the pull imply a high paraboloid error due to insufficient paraboloid fits of the likelihood minima.

6.2.3 PDOM vs. mDOM

In the following, a comparison is drawn between the previously individually presented reconstructions of the PDOM and mDOM. In fig. 6.13, plots of the true error $\Delta\Psi$ and the pull $\frac{\Delta\Psi}{\sigma}$ over energy with the Poisson and extended unbinned likelihood reconstructions for PDOM and mDOM can be found.
First of all, it can be stated that, mostly, the mDOM reconstructions yield smaller

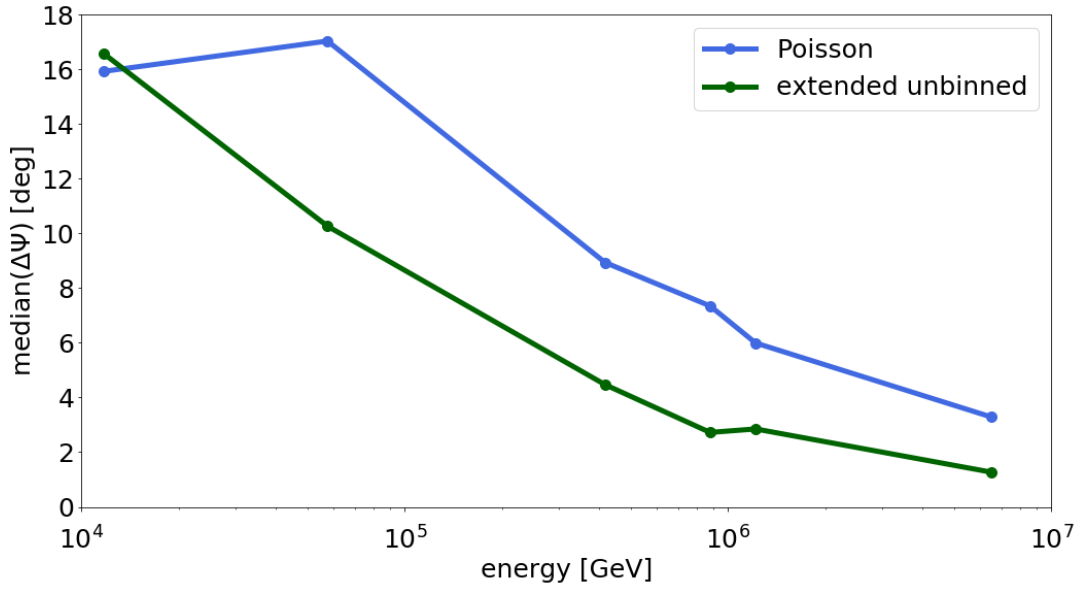

(a)

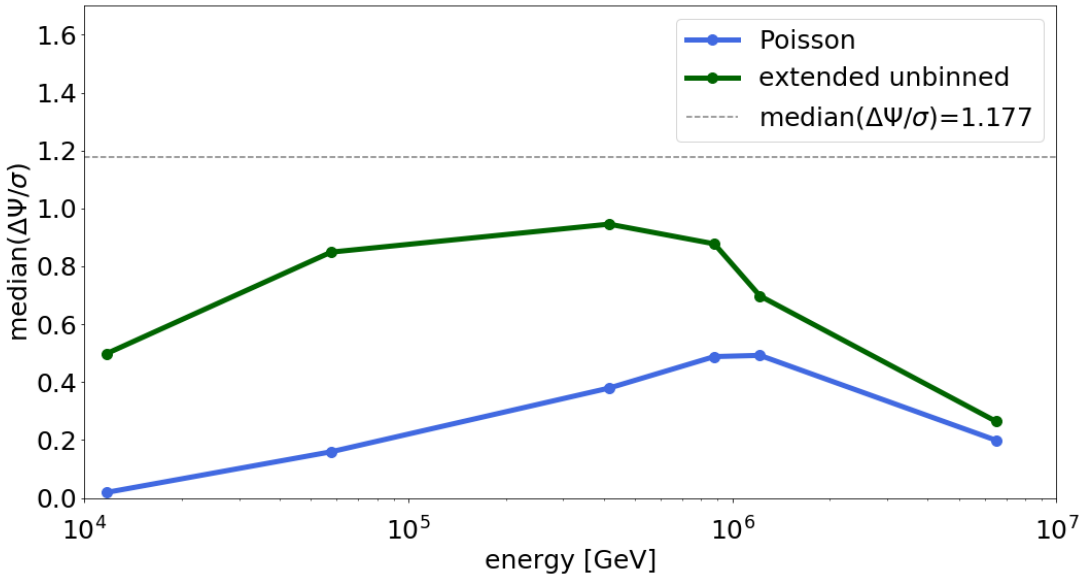

(b)

Figure 6.9: (**a**) True error $\Delta\Psi$ & (**b**) pull $\frac{\Delta\Psi}{\sigma}$ over event energy for the **PDOM** Poisson (**blue**) and extended unbinned (**green**) likelihood reconstructions, applied to the idealized pulses. Ideal pull median value of 1.177 is plotted in **grey**.

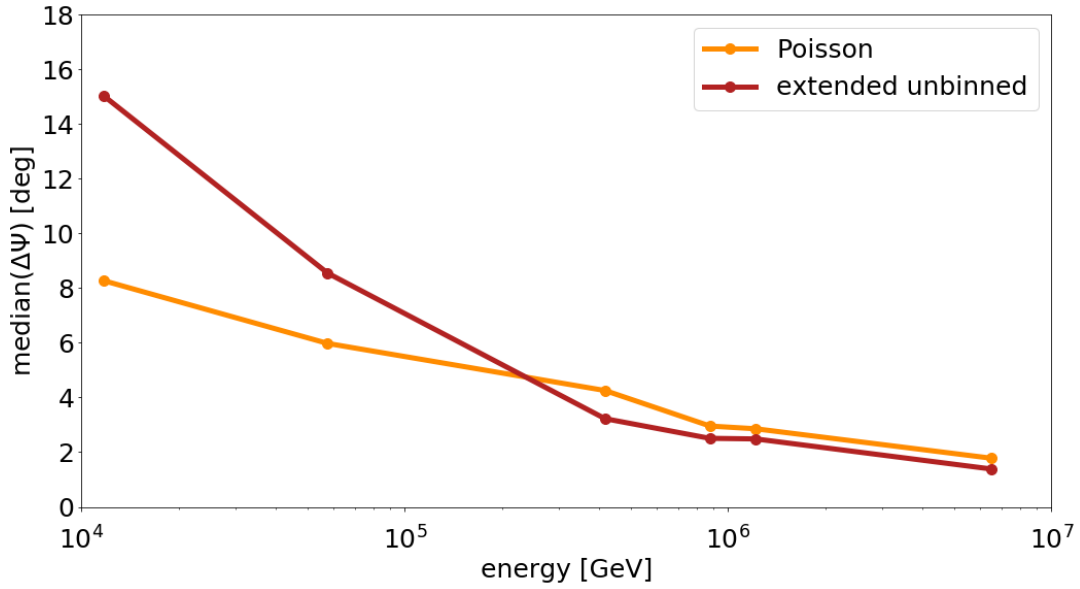

(a)

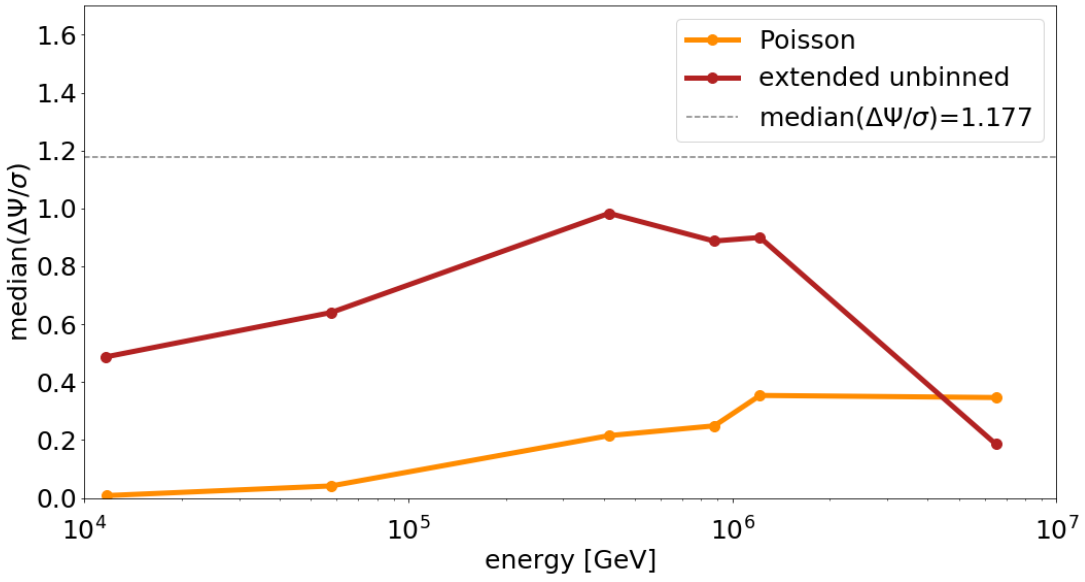

(b)

Figure 6.10: (**a**) True error $\Delta\Psi$ & (**b**) pull $\frac{\Delta\Psi}{\sigma}$ over event energy for the **mDOM** Poisson (**orange**) and extended unbinned (**red**) likelihood reconstructions, applied to the idealized pulses. Ideal pull median value of 1.177 is plotted in **grey**.

angular errors $\Delta\Psi$ than the PDOM reconstructions. This applies for both likelihood approaches, even though the results of the PDOM extended unbinned reconstruction align with the outcome of the mDOM extended unbinned and turn out better than the results of mDOM Poisson reconstruction in the higher energy regimes. Furthermore, the true error plot shows in the low energy range that the mDOM Poisson likelihood provides the smallest angular difference between true and reconstructed direction of all tested reconstruction methods. For the lowest energy bin 10 – 50 TeV, the extended unbinned method for the mDOM slightly outperforms both PDOM approaches. Over the course of the curve up to the 100 – 500 TeV bin, the difference between the extended unbinned likelihoods of PDOM and mDOM is approximately constant at values around 1.3° – 1.7° while the distance between these two curves and the Poisson likelihood curve of the PDOM enlarges to a maximum of roughly 7° – 9°. For the highest reconstructed event energies a true error median of approximately 1.8° could be obtained through the Poisson likelihood for the mDOM while through extended unbinned approach for PDOM and mDOM roughly 1.3° & 1.4°. The Poisson likelihood for the PDOM decreases with higher energies only down to $\sim 3.3°$. The values of $\Delta\Psi$ for each energy bin are entered in table 6.3.
In order to put the medians of the true errors $\Delta\Psi$ into perspective, the 14% and 86% quantiles of each bin for the different reconstructions were computed. The corresponding plots which can be found in fig. 6.11 for the Poisson reconstructions and in fig. 6.12 for the extended unbinned reconstructions of each DOM display the area between the respective two quantiles marked in color. The 14% quantile limits thereby the top while the 86% quantile restricts the bottom of the colored area. The previous observations that the mDOM yields smaller $\Delta\Psi$ in the used reconstruction than the PDOM are basically confirmed by the plots. This is reflected in the Poisson reconstructions by the clearly smaller 86% quantiles of the mDOM reconstruction compared to the PDOM 86% quantiles. The same behavior is recognizable for the 14% quantiles but not quite as significant. In the case of the extended unbinned reconstructions, the 86% quantile curves lie closer to each other such that only tendencies are recognizable which imply a slightly smaller curve for the mDOM over all energy bins except for the first one. Here, the 86% median of the PDOM extended unbinned approach yields better true errors. For the 14% quantiles no significant difference is visible between PDOM and mDOM.
The expectations of the pull $\frac{\Delta\Psi}{\sigma}$ mostly couldn't be fulfilled by neither the PDOM nor the mDOM reconstructions. This includes the non-constant behavior of all curves which falls off for the low and high energy bins, except in the case of the mDOM Poisson likelihood. Here, the curve is approximately constant for the two highest energy bins. The courses of the PDOM and mDOM pulls resemble for each of the both likelihoods while the extended unbinned curves lie above the Poisson curves. Furthermore, the pull values which are overall too small compared to the ideal value of 1.177 have to be mentioned. These imply large paraboloid errors for all reconstructions while merely the pull values in the mid-energy regime of the extended unbinned reconstructions for PDOM and mDOM fall in a range near the optimum.

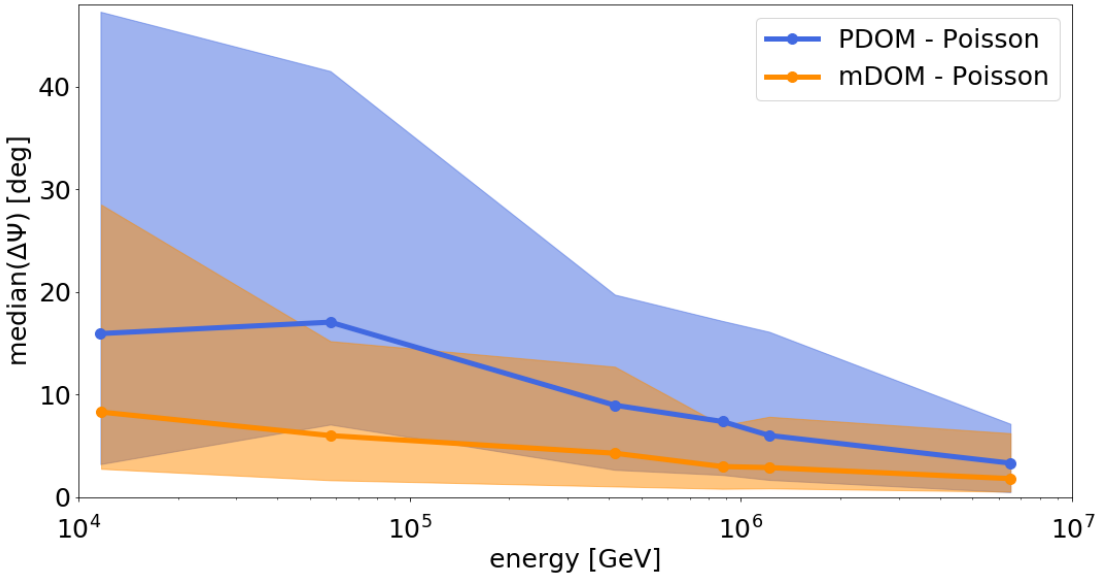

Figure 6.11: True error median $\Delta\Psi$ with 14% and 86% quantiles enclosing the colored areas, over event energy for the PDOM (**blue**) & mDOM (**orange**) Poisson reconstructions with the idealized pulses. The respective medians of $\Delta\Psi$ are represented by the continuous lines in the corresponding colors.

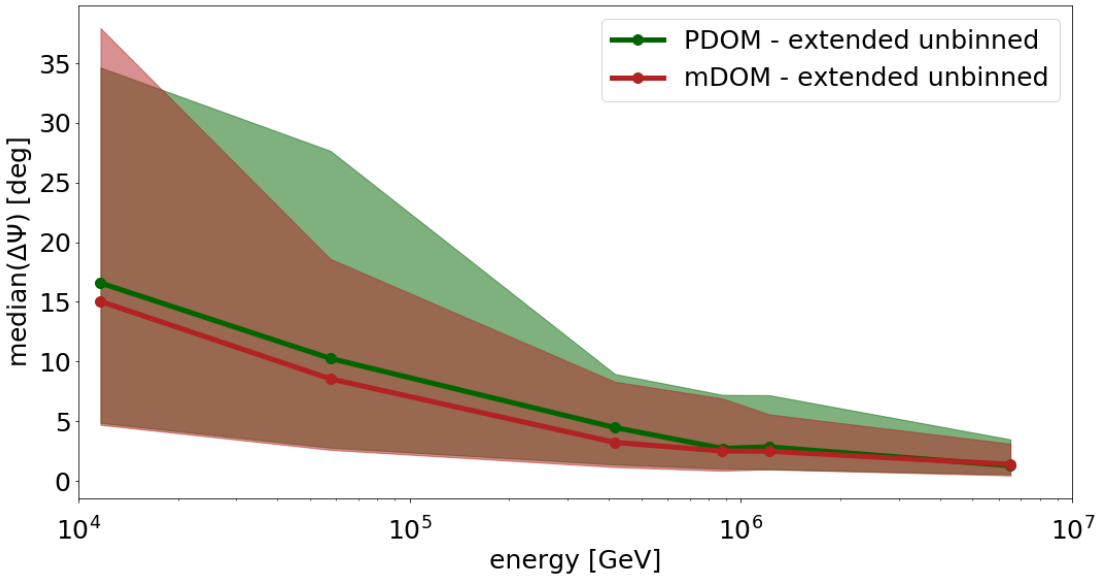

Figure 6.12: True error median $\Delta\Psi$ with 14% and 86% quantiles enclosing the colored areas over event energy for the PDOM (**green**) & mDOM (**red**) extended unbinned reconstructions with the idealized pulses. The respective medians of $\Delta\Psi$ are represented by the continuous lines in the corresponding colors.

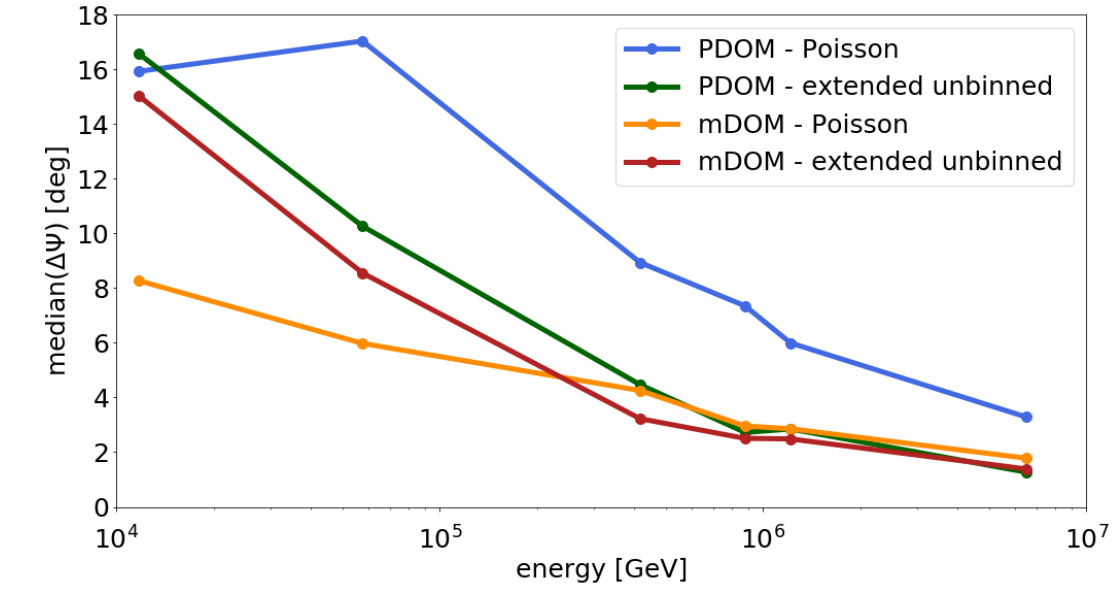

(a)

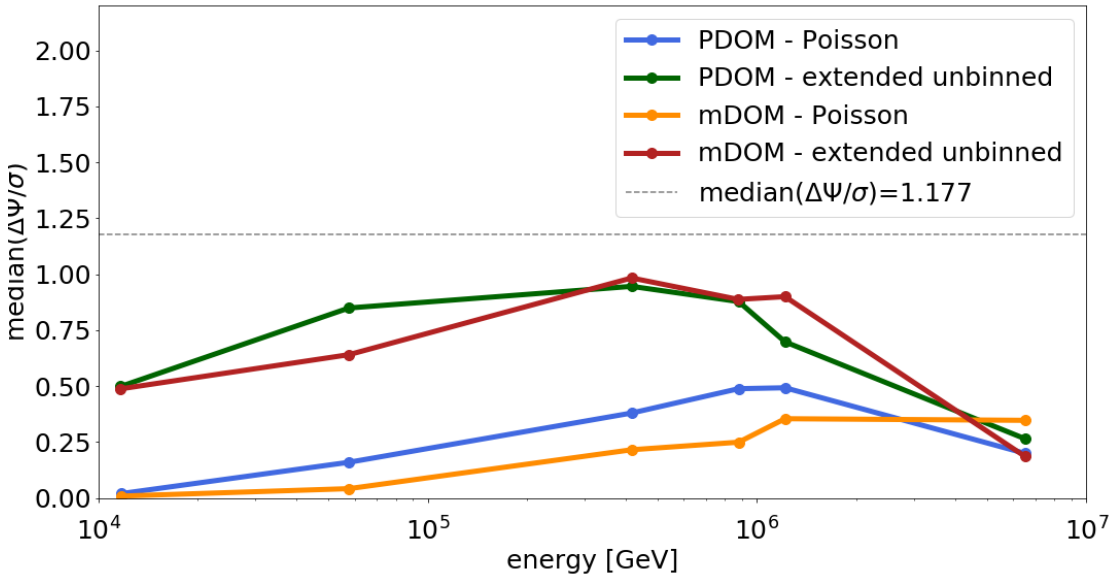

(b)

Figure 6.13: (**a**) True error $\Delta\Psi$ & (**b**) pull $\frac{\Delta\Psi}{\sigma}$ over event energy for the **PDOM** as well as the **mDOM** likelihood reconstructions, applied to the idealized pulses.Ideal pull median value of 1.177 is plotted in **grey**.

energy bin	$\Delta\Psi_{\text{PDOM,Poisson}}$	$\Delta\Psi_{\text{PDOM,unbinned}}$	$\Delta\Psi_{\text{mDOM,Poisson}}$	$\Delta\Psi_{\text{mDOM,unbinned}}$
10 – 50 TeV	15.9°	16.6°	8.3°	15.0°
50 – 100 TeV	17.0°	10.3°	6.0°	8.6°
100 – 500 TeV	8.9°	4.5°	4.3°	3.2°
500 TeV – 1 PeV	7.3°	2.7°	3.0°	2.5°
1 – 5 PeV	6.0°	2.8°	2.9°	2.5°
5 – 10 PeV	3.3°	1.3°	1.8°	1.4°

Table 6.3: Rounded true error medians for the neutrino energy bins of the dataset where $\Delta\Psi_{\text{PDOM,Poisson}}, \Delta\Psi_{\text{PDOM,unbinned}}$ denote the true error median for the Poisson and extended unbinned likelihood approaches of the PDOM reconstructions while $\Delta\Psi_{\text{mDOM,Poisson}}, \Delta\Psi_{\text{mDOM,unbinned}}$ denote the true error median for the Poisson and extended unbinned likelihood approaches of the mDOM reconstructions.

7 Conclusion

In this thesis, shower events for the proposed Gen2 optical modules PDOM and mDOM were reconstructed. Concretely, this was done for 600 events over an energy range of 10 TeV – 10 PeV. The dataset was obtained through three cuts. The first one was an energy selection, leading to six half decades in the previously stated energy range. A second cut was given by the requirement that the number of triggered standard IceCube DOMs in the IC-86 array by an event is smaller than 50 in order to accept only events which are located in Gen2. Lastly, it was demanded that the events should trigger at least four Gen2 strings, and therefore deploy a sufficient number of photons in Gen2 for the event reconstruction. The used reconstruction methods are based on the Maximum-Likelihood-Estimation with two different likelihood function approaches: the extended unbinned likelihood, where amplitude and time information enters, and the Poisson likelihood where only the overall amplitude is taken into account. These reconstructions were mostly performed on idealized light pulses as the realistic pulses showed unexpected and faulty behavior which is an issue that has to be addressed in the future. In order to allow a fair comparison between PDOM and mDOM, the number of photons detected by the PDOM was scaled up by a factor of 2.2 to compensate its smaller effective photo cathode area.
It was shown that the reconstructions work on a basic level for the idealized and the realistic pulses of a pure mDOM Gen2 High-Energy Array by examining the likelihood scans of four example events in the low energy regime. Here, the likelihoods showed smooth behavior although the Poisson reconstructions provided mostly smaller angular errors $\Delta\Psi$ between the true direction and the reconstructed direction than the extended unbinned approach. This observation contrasts with the expectation that the extended unbinned formulation should yield better true errors than the Poisson one due to higher amount of information an unbinned approach inherits. It was therefore investigated if this behavior is a result of a minimization problem where only a local minimum instead of a global minimum is found. This assumption couldn't be verified by testing two different minimization procedures with more minimization steps and different numeric minimizers. It remains thus an unsolved problem which has to be examined in future studies.
The reconstructions on the PDOM light pulses showed the expected behavior concerning the angular error $\Delta\Psi$. Here, both likelihood approaches improved with increasing energy and the extended likelihood approach yielded smaller $\Delta\Psi$ medians compared to the Poisson likelihood reconstruction with exception of the lowest energy bin 10 TeV – 50 TeV which shows the opposite, but can be statistical fluctuation. The mDOM reconstructions display the same decreasing behavior of the true error over increasing energies. However, the Poisson reconstruction provides unexpected smaller angular errors than the extended

unbinned reconstructions for the three energy bins 10 TeV – 50 TeV, 50 TeV – 100 TeV & 100 TeV – 500 TeV. This observation coincides with the observations of the mDOM likelihood scans for the test events and stay an issue which has to be investigated in the future.
The results show that the mDOM reconstructions provide up to $\sim 50\%$ smaller angular errors than the PDOM reconstructions for both likelihood approaches which could be confirmed for the Poisson approach while the extended unbinned likelihood showed mostly the same tendencies under consideration of the 14% & 86% quantils. All reconstruction approaches start at the 10 TeV – 50 TeV bin with a true error median of roughly 15° – 17°, except the mDOM Poisson likelihood which provides a remarkable $\sim 8°$ true error median in this lowest energy bin. With increasing energies, the angular error medians improve for the reconstructions and align above 1 PeV while providing angular error medians of 1° – 2° at the 5 PeV – 10 PeV bin. Merely the PDOM Poisson likelihood true error curve doesn't align and delivers a true error median of $\sim 3°$ in the highest energy bin.
Furthermore, the pull for the reconstructions was investigated. All of the pull curves don't show the expected constant behavior over energy, increase with the energy and fall off or stay only constant for the highest energies. The values of the pull were for all reconstructions smaller than the theoretically motivated value of 1.177, especially for the Poisson reconstruction approach of both optical modules. This indicates a high paraboloid error as probably a result of bad paraboloid fits in the estimation process of σ. However, these high errors are currently not fully understood and their correction remains a task of the future.
Overall, these are the first results for cascade directional reconstructions with the mDOM. They indicate, that under idealized conditions, the mDOM performs qualitatively in line with the expectations. In the future, it will be important to handle realistic photon propagation, correct the uncertainty estimation, and identify the problem with the extended unbinned likelihood.

References

[1] M. G. Aartsen, K. Abraham, M. Ackermann, J. Adams, J. A. Aguilar, M. Ahlers, M. Ahrens, D. Altmann, K. Andeen, T. Anderson, and et al. All-sky Search for Time-integrated Neutrino Emission from Astrophysical Sources with 7 yr of IceCube Data. *Astrophys. J.*, 835:151, February 2017.

[2] M. G. Aartsen, M. Ackermann, J. Adams, J. A. Aguilar, M. Ahlers, M. Ahrens, D. Altmann, K. Andeen, T. Anderson, I. Ansseau, and et al. The IceCube Neutrino Observatory: instrumentation and online systems. *Journal of Instrumentation*, 12:P03012, March 2017.

[3] M. G. Aartsen, M. Ackermann, J. Adams, J. A. Aguilar, M. Ahlers, M. Ahrens, I. A. Samarai, D. Altmann, K. Andeen, T. Anderson, and et al. Search for Astrophysical Sources of Neutrinos Using Cascade Events in IceCube. *Astrophys. J.*, 846:136, September 2017.

[4] M. Agostini, K. Altenmüller, S. Appel, and V. et. al Atroshchenko. Limiting neutrino magnetic moments with Borexino Phase-II solar neutrino data. *Phys. Rev.*, 96(9):091103, November 2017.

[5] Roger Barlow. Extended maximum likelihood. *Nuclear Instruments and Methods in Physics Research Section A: Accelerators, Spectrometers, Detectors and Associated Equipment*, 297(3):496 – 506, 1990.

[6] Julia K. Becker. High-energy neutrinos in the context of multimessenger astrophysics. *Physics Reports*, 458(4):173 – 246, 2008.

[7] A. R. Bell. The acceleration of cosmic rays in shock fronts – i. *Monthly Notices of the Royal Astronomical Society*, 182(2):147–156, 1978.

[8] J. Blümer, R. Engel, and J. R Hörandel. Cosmic rays from the knee to the highest energies. *Progress in Particle and Nuclear Physics*, 63:293–338, 2009. `http://particle.astro.ru.nl/pub/JPPNP63-293.pdf`.

[9] C.-Y. Chen, P. S. B. Dev, and A. Soni. Standard model explanation of the ultrahigh energy neutrino events at IceCube. *Physical Review D*, 89(3):033012, February 2014.

[10] L. Classen. *The mDOM - a multi-PMT digital optical module for the IceCube-Gen2 neutrino telescope*. PhD thesis, Friedrich-Alexander-Universität Erlangen-Nürnberg, 2017.

[11] L. F. Curtiss. Deflection of cosmic rays by a magnetic field. *Bureau of Standards Journal of Research*, 9:815–823, 1930.

[12] NLopt Documentation. Nlopt algorithms. `https://nlopt.readthedocs.io/en/latest/NLopt_Algorithms/`. Access: 2018-07-03.

[13] C.F. Dormann. *Parametrische Statistik: Verteilungen, maximum likelihood und GLM in R*. Statistik und ihre Anwendungen. Springer Berlin Heidelberg, 2017.

[14] D. Fargion, P. Oliva, and G. Ucci. Why not any tau double bang in Icecube, yet? *ArXiv e-prints*, December 2015.

[15] E Fermi. On the origin of the cosmic radiation. *Physical Review*, 75(8), 1949. `https://journals.aps.org/pr/pdf/10.1103/PhysRev.75.1169`.

[16] R. Fletcher. A new approach to variable metric algorithms. *The Computer Journal*, 13(3):317–322, 1970.

[17] D. Foreman-Mackey, D. W. Hogg, D. Lang, and J. Goodman. emcee: The mcmc hammer. *PASP*, 125:306–312, 2013.

[18] J. A. Formaggio and G. P. Zeller. From ev to eev: Neutrino cross sections across energy scales. *Rev. Mod. Phys.*, 84:1307–1341, Sep 2012. `https://link.aps.org/doi/10.1103/RevModPhys.84.1307`.

[19] Thorsten Glüsenkamp. *Search for a cumulative neutrino flux from 2LAC-blazar populations using 3 years of IceCube data*. PhD thesis, Humboldt-Universität zu Berlin, 2016.

[20] A. Goldschmidt. Scientific goals of the icecube neutrino detector at the south pole. *Nuclear Physics B - Proceedings Supplements*, 110:516 – 518, 2002.

[21] Jonathan Goodman and Jonathan Weare. Ensemble samplers with affine invariance. *Commun. Appl. Math. Comput. Sci.*, 5(1):65–80, 2010.

[22] S. Grullon, D. J. Boersma, and G. Hill. Photonics-based log-likelihood reconstruction in icecube. `https://icecube.wisc.edu/~grullon/Reconstruction_Internal.pdf`, June 2008.

[23] F. Halzen and S. R. Klein. Invited Review Article: IceCube: An instrument for neutrino astronomy. *Review of Scientific Instruments*, 81(8):081101–081101, August 2010.

[24] V. F. Hess. Über beobachtungen der durchdringenden strahlung bei sieben freiballonfahrten. Z. Phys. 13 (1912) 1084. `http://cds.cern.ch/record/262750`.

[25] A. M. Hillas. Cosmic Rays: Recent Progress and some Current Questions. *ArXiv Astrophysics e-prints*, July 2006. http://adsabs.harvard.edu/abs/2006astro.ph..7109H.

[26] K. D. Hoffman. High energy neutrino telescopes. *New Journal of Physics*, 11(5):055006, May 2009.

[27] IceCube Software Documentation Homepage. Detectorsim. http://software.icecube.wisc.edu/documentation/projects/simprod-scripts/segments/detector.html#id4. Access: 2018-06-24.

[28] IceCube Software Documentation Homepage. icecube.filterscripts package. http://software.icecube.wisc.edu/documentation/python/icecube.filterscripts.html?highlight=baseproc#module-icecube.filterscripts.baseproc. Access: 2018-06-24.

[29] IceCube Software Documentation Homepage. icecube.vuvuzela package. http://software.icecube.wisc.edu/documentation/python/icecube.vuvuzela.html?highlight=vuvuzela#module-icecube.vuvuzela. Access: 2018-06-24.

[30] IceCube Software Documentation Homepage. simclasses c++ api reference. http://software.icecube.wisc.edu/documentation/doxygen/simclasses/index.html?highlight=mcpe#structI3MCPE. Access: 2018-06-24.

[31] IceCube Software Documentation Homepage. Vuvuzela. http://software.icecube.wisc.edu/documentation/projects/vuvuzela/index.html. Access: 2018-06-29.

[32] IceCube Collaboration. Evidence for High-Energy Extraterrestrial Neutrinos at the IceCube Detector. *Science*, 342:1242856, November 2013.

[33] IceCube-Gen2 Collaboration, :, M. G. Aartsen, M. Ackermann, J. Adams, J. A. Aguilar, M. Ahlers, M. Ahrens, D. Altmann, T. Anderson, and et al. IceCube-Gen2: A Vision for the Future of Neutrino Astronomy in Antarctica. *ArXiv e-prints*, December 2014.

[34] IceProd. Dataset 20030 details. https://iceprod2.icecube.wisc.edu/dataset/O1r99c57luMXk0, 2017. Access: 2018-06-24.

[35] U. F. Katz and C. Spiering. High-energy neutrino astrophysics: Status and perspectives. *Progress in Particle and Nuclear Physics*, 67:651–704, July 2012.

[36] T. Kittler. Personal communication.

[37] Jürgen Knödlseder. The future of gamma-ray astronomy. *Comptes Rendus Physique*, 17(6):663 – 678, 2016. Gamma-ray astronomy / Astronomie des rayons gamma - Volume 2.

[38] Ladislav Lukšan and Emilio Spedicato. Variable metric methods for unconstrained optimization and nonlinear least squares. *Journal of Computational and Applied Mathematics*, 124(1):61 – 95, 2000. Numerical Analysis 2000. Vol. IV: Optimization and Nonlinear Equations.

[39] D. Meschede. *Gerthsen Physik*. Springer-Lehrbuch. Springer Berlin Heidelberg, 2015.

[40] E Middell, J McCartin, and M D'Agostino. Improved reconstruction of cascade-like events in icecube. *PROCEEDINGS OF THE 31st ICRC*, 2009.

[41] T. Neunhöffer. Estimating the angular resolution of tracks in neutrino telescopes based on a likelihood analysis. *Astroparticle Physics*, 25:220–225, April 2006.

[42] Piti Ongmongkolkul. iminuit - api. `http://iminuit.readthedocs.io/en/latest/api.html`. Access: 2018-07-03.

[43] C. Patrignani and Particle Data Group. Review of particle physics. *Chinese Physics C*, 40(10):100001, 2016.

[44] P. Pfaff, C. Plagemann, and W. Burgard. Improved likelihood models for probabilistic localization based on range scans. `http://www2.informatik.uni-freiburg.de/~pfaff/downloads/pfaff07iros.pdf`.

[45] M. J. D. Powell. The bobyqa algorithm for bound constrained optimization without derivatives. 2009.

[46] S. Sahu and B. Zhang. On the non-detection of Glashow resonance in IceCube. *ArXiv e-prints*, December 2016.

[47] Perry Sandstrom and IceCube-PINGU Collaboration. Digital optical module design for pingu. *AIP Conference Proceedings*, 1630(1):180–183, 2014.

[48] C. Spiering. Towards high-energy neutrino astronomy. A historical review. *European Physical Journal H*, 37:515–565, August 2012.

[49] The IceCube-Gen2 Collaboration, :, M. G. Aartsen, K. Abraham, M. Ackermann, J. Adams, J. A. Aguilar, M. Ahlers, M. Ahrens, D. Altmann, and et al. IceCube-Gen2 - The Next Generation Neutrino Observatory at the South Pole: Contributions to ICRC 2015. *ArXiv e-prints*, October 2015.

[50] D. Xu and IceCube Collaboration. Exploring the Universe with Neutrinos: Recent Results from IceCube. *Nuclear and Particle Physics Proceedings*, 287:139–142, June 2017.

List of Figures

Acknowledgement

First, I would like to thank Prof. Dr. Gisela Anton and Dr. Thorsten Glüsenkamp for giving me the opportunity to write this thesis, and therefore contribute to IceCube.
I also want to thank all the people from the ECAP IceCube group who warmly welcomed me and made it easy for me to integrate. Hereby, I'd like to point out Thorsten Glüsenkamp who overtook the supervision for this thesis. Especially, I want to dedicate a huge thank to Thomas Kittler and Gerrit Wrede for helping me with numerous questions about IceCube and scientific programming as well as their proof reading. Furthermore, I'd like to express my appreciation for many discussion concerning not only the topics of this thesis but also other branches of physics and everyday life.

Last and most importantly, I'd like to thank my family and friends for supporting me and enabling me to achieve my goals and aspirations.

Erklärung

Hiermit erkläre ich, dass die vorliegende Arbeit **„IceCube-Gen2 cascade reconstruction studies with the PDOM and mDOM“** von mir eigenständig und nur unter Zurhilfenahme der angegebenen Quellen und bereitgestellten Hilfsmittel angefertigt wurde.

Erlangen, 13.07.2018
Ort, Datum

Sebastian Spiegel